Supplementary Material (ESI) for Chemical Communications

Chemical Communications

Supporting Information

Can Terdentate 2,6-Bis(1,2,3-Triazol-4-yl)Pyridines form Stable Coordination Compounds?

Yongjun Li,[a] *John C. Huffman,*[a,b] *Amar H. Flood*[a]*

[a] Chemistry Department, Indiana University, 800 East Kirkwood Avenue, Bloomington, IN 47405

[b] Molecular Structure Center, Indiana University

Table of Contents

S.1. EXPERIMENTAL

General

All reagents were obtained from commercial sources and used as received unless otherwise noted. The compounds 2,6-diethynylpyridine, [1] 3-azidopropan-1-ol, [2] 1-azidobutane [3] and $Ru(DMSO)_4Cl_2$[4] were prepared according to literature procedures. Column chromatography was performed on silica gel (160 – 200 mesh), and thin-layer chromatography (TLC) was performed on precoated silica gel plates (0.25 mm thick, $60F_{254}$, Merck, Germany) and observed under UV light. Nuclear magnetic resonance (NMR) spectra were recorded on Varian Inova (400 MHz), Varian Vxr (400 MHz) and Varian Gemini (300 MHz) spectrometers at room temperature (298 K). Chemical shifts were reported versus tetramethylsilane and referenced to the residual solvent peaks. High resolution chemical ionization (CI) and electrospray ionization (ESI) mass spectrometry were performed on a Thermo Electron Corporation MAT 95XP-Trap mass spectrometer. UV-Vis spectra were measured on a Varian Cary 5000 UV-Vis-NIR spectrophotometer. FT-IR spectra were recorded on a Nicolet 510P FT-IR Spectrometer with EZ OMNIC E.S.P. software. Elemental analyses (CHN) were performed at the Robertson Microlit Laboratories.

Safety Comment: **Sodium azide is very toxic, personal protection precautions should be taken. As low molecular weight organic azides and ClO_4^- salts are potential explosives, care must be taken during their handling. Generally, when the total number of carbon (N_C) plus oxygen (N_O) atoms is less than the total numbers of nitrogen atoms (N_N) by a ratio of three, i.e., $(N_C + N_O) / N_N < 3$, the compound is considered as an explosive hazard. In those instances, the compound was prepared prior to use and used immediately. A standard PVC blast shield was used when necessary.**

Electrochemistry

Cyclic voltammetry (CV) was performed using a Princeton Applied Research potentiostat/galvanostat model 263A. Anhydrous MeCN (Aldrich) was used as the solvent under inert atmosphere (Ar) and 0.1 M tetra(*n*-butyl)ammonium hexafluorophosphate ($TBAPF_6$) was used as the supporting electrolyte. The $TBAPF_6$ was recrystallized twice from EtOH. A glassy

carbon rod was used as the working electrode, a platinum wire was used as the counter electrode, and a silver wire was used as a pseudoreference electrode. The redox potentials are reported relative to the standard calomel electrode (SCE) redox couple and these calibrated data were obtained by addition of the SCE to the solution at the end of the experiments.

X-ray Crystallography

Data Collection: Diffraction data for $[Fe(\mathbf{1})_2]\bullet 2PF_6$, $[Ru(\mathbf{1})_2]\bullet 2PF_6$ and $[Eu(\mathbf{2})_3]\bullet 3ClO_4$ were collected at 177, 125 and 135 K, respectively. The data sets were collected on a Bruker SMART 6000 CCD diffractometer. A preliminary set of cell constants was calculated from reflections obtained from three nearly orthogonal sets of 30, 20 and 30 frames, respectively. The data collection was carried out using graphite monochromated Mo Kα radiation with a frame time of 15, 15 and 30 s, respectively, and a detector distance of 5.0 cm. A randomly oriented region of a sphere in reciprocal space was surveyed. Three sections of 606 frames were collected with 0.30º steps in ω at different ϕ settings with the detector set at –43° in 2θ. The intensity data for $[Eu(\mathbf{2})_3]\bullet 3ClO_4$ were corrected for absorption (SADABS).[5] Final cell constants were calculated from the *xyz* centroids of 872 ($[Fe(\mathbf{1})_2]\bullet 2PF_6$), 1965 ($[Ru(\mathbf{1})_2]\bullet 2PF_6$) or 2045 ($[Eu(\mathbf{2})_3]\bullet 3ClO_4$) strong reflections from the actual data collection after integration (SAINT).[6]

Structure Solution and Refinement: Intensity statistics and systematic absences suggested the centrosymmetric space group C2/c ($[Fe(\mathbf{1})_2]\bullet 2PF_6$), $P2_1/c$ ($[Ru(\mathbf{1})_2]\bullet 2PF_6$) and the orthorhombic centrosymmetric space group Pbcn ($[Eu(\mathbf{2})_3]\bullet 3ClO_4$), and subsequent solution and refinement confirmed these choices. The structure was solved (Table S1) using SHELXS–97 and refined with SHELXL-97.[7] A direct-methods solution was calculated which provided most non-hydrogen atoms from the *E*-map. Full-matrix least squares / difference Fourier cycles were performed which located the remaining non-hydrogen atoms. All non-hydrogen atoms were refined with anisotropic displacement parameters. For $[Fe(\mathbf{1})_2]\bullet 2PF_6$, one peak was located near a center of inversion and arises from the partial occupancy by a molecule of H_2O. Two other crystals were examined in an attempt to better characterize the solvent, but to no avail. For both $[Fe(\mathbf{1})_2]\bullet 2PF_6$ and $[Ru(\mathbf{1})_2]\bullet 2PF_6$, all hydrogen atoms were located in subsequent Fourier maps and included as isotropic contributors in the final cycles of refinement. For $[Eu(\mathbf{2})_3]\bullet 3ClO_4$, there are four independent perchlorate groups, two lying on symmetry elements, and there is some

disorder in two of the perchlorate groups, and two of the *n*-butyl chains are disordered. In addition, there is a single peak located at (0.91, 0.12, 0.79) that lies nearly 3 Å from any other non-hydrogen atom. It was assumed to be an oxygen atom from a water solvent in the refinement. All hydrogen atoms were located in subsequent Fourier maps and included as isotropic contributors in the final cycles of refinement. The 50% thermal ellipsoids for each crystal structure are shown in Figure S1.

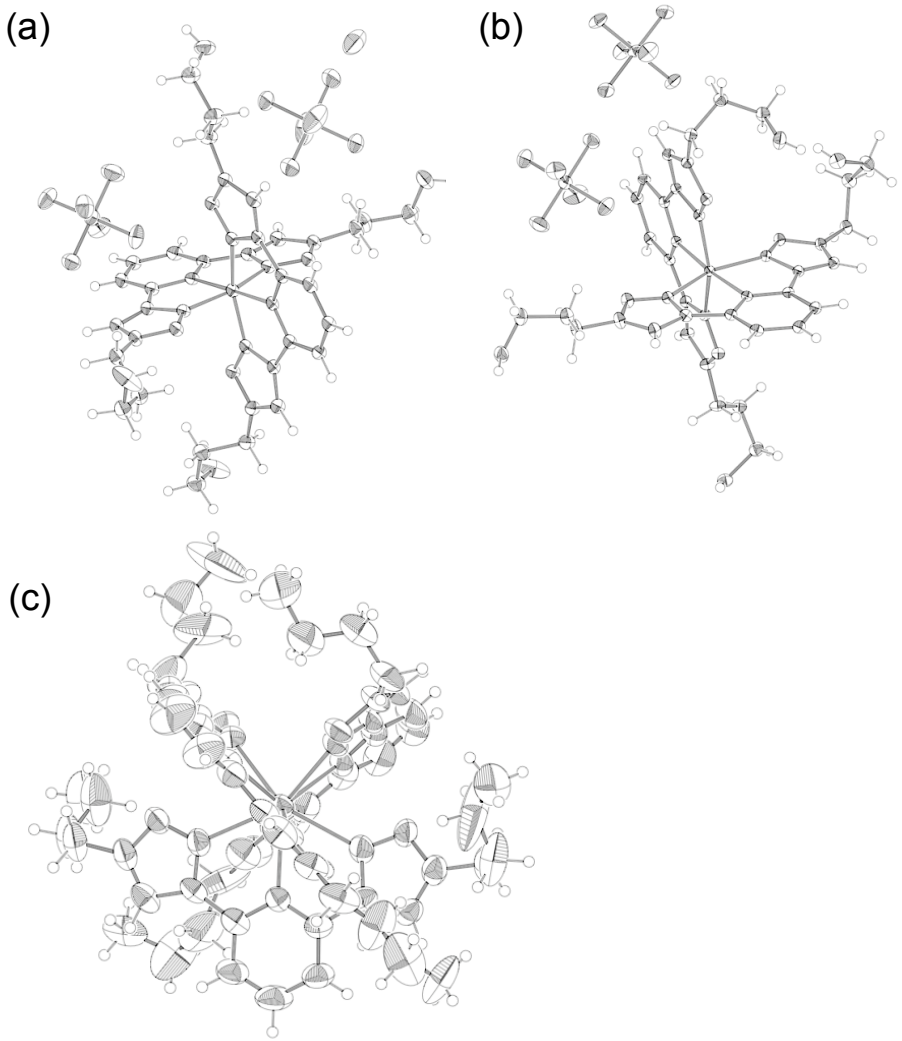

Figure S1. 50% Ellipsoids of (a) [Fe(**1**)$_2$]•2PF$_6$, (b) [Ru(**1**)$_2$]•2PF$_6$ and (c) [Eu(**2**)$_3$]•3ClO$_4$.

Table S1. A summary of the refinement details and the resulting factors for $[Fe(\mathbf{1})_2]\cdot 2PF_6$, $[Ru(\mathbf{1})_2]\cdot 2PF_6$ and $[Eu(\mathbf{2})_3]\cdot 3ClO_4$.

Empirical Formula:	$C_{30}H_{38}F_{12}FeN_{14}O_4P_2$	$C_{30}H_{38}F_{12}N_{14}O_4P_2Ru$	$C_{51}H_{71}Cl_3EuN_{21}O_{13}$
Color of Crystal:	orange	yellow	colorless
Crystal System:	Monoclinic	Monoclinic	Orthorhombic
Space Group:	C2/c	P2(1)/c	Pbcn
Crystal size:	0.26 × 0.18 × 0.11 mm	0.35 × 0.20 × 0.12 mm	0.30 × 0.25 × 0.10 mm
Instrument:		IUMSC SMART6000	
Cell Dimensions			
Data	872 reflections; 173 K	1965 reflections; 125 K	2045 reflections; 135 K
a =	11.156(3)	12.2491(8)	19.2068(17)
b =	26.836(3)	23.2119(15)	28.499(3)
c =	14.153(3)	14.9526(10)	24.321(2)
alpha =	90	90	90
beta =	104.726(5)	108.375(2)	90
gamma =	90	90	90
Z (Molecules/Cell):	4	4	8
Volume:	4097.98(16)	4034.6(5)	13313(2)
Calculated Density:	1.657	1.728	1.441
Molecular Weight:	1022.51	1049.75	1444.60
Linear Abs. Coef.:	0.556	0.580	1.136
Final Residuals:			
R(F) =	0.042	0.0299	0.0638
Rw(F) =	0.102	0.0729	0.1915

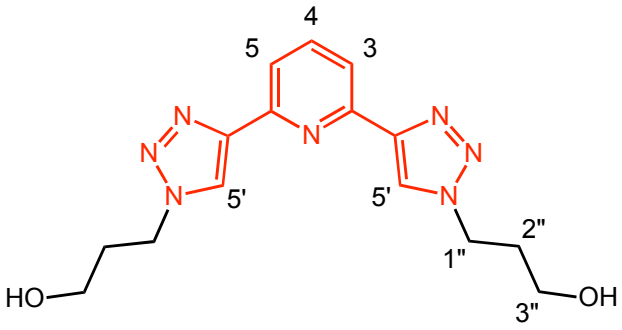

2,6-bis(1-propan-1-ol-1,2,3-triazol-4-yl)pyridine, 1: A solution of 2,6-diethynylpyridine (1 mmol, 127 mg), 3-azidopropan-1-ol (2.2 mmol, 222 mg, (N_C + N_O) / N_N = 1.3; ***potentially explosive***), sodium ascorbate (0.2 mmol, 44.6 mg), and $CuSO_4$ (0.02 mmol, 5.6 mg) in a 1:1 mixture of EtOH:H_2O (14 mL) was stirred at room temperature for 24 h. After removal of the solvents in vacuo, the crude product was purified by column chromatography (CH_2Cl_2:MeOH, 3:1) to afford **1** (309 mg, 94%). ^{1}H NMR (CD_3COCD_3, 400 MHz), δ = 8.50 (s, 2H), 8.03 (d, 2H, J = 7.6 Hz), 7.96 (t, 1H, J = 7.6 Hz), 4.61 (t, 4H, J = 6.8 Hz), 3.83 (s, br, 2H), 3.63 (s, br, 4H), 2.20~2.14 (m, 4H). ^{13}C NMR (CD_3COCD_3, 75 MHz), δ = 152.4, 149.6, 139.5, 124.8, 120.1, 59.9, 48.9, 34.9. IR (KBr) ν = 3336, 3161, 3122, 2955, 2908, 2877, 1607, 1577, 1455, 1414, 1334, 1230, 1200, 1076, 1045, 812 cm^{-1}. MS (HiResEI) Cald for $C_{15}H_{20}N_7O_2$(M+H) 330.1673; Found 330.1676. Anal. Calcd for $C_{15}H_{19}N_7O_2$: C, 54.70; H, 5.81; N, 29.77. Found: C, 54.59; H, 5.80; N, 29.46.

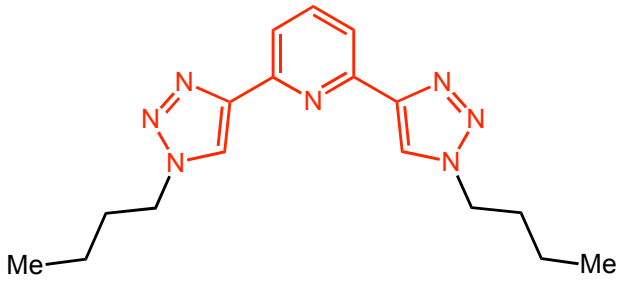

2,6-bis(1-butyl-1*H*-1,2,3-triazol-4-yl)pyridine, 2: A solution of 2,6-diethynylpyridine (0.5 mmol, 64 mg), 1-azidobutane (1.1 mmol, 109 mg, (N_C + N_O) / N_N = 1.3l; ***potentially explosive***), sodium ascorbate (0.1 mmol, 222.3 mg), and $CuSO_4$ (0.01 mmol, 2.8 mg) in a 1:1 mixture of EtOH:H_2O (10 mL) was stirred at room temperature for 24 h. After removal of the solvents under vacuum, the crude product was purified by column chromatography (CH_2Cl_2:MeOH, 3:1) to afford **2** (156 mg, 96%). ^{1}H NMR ($CDCl_3$, 400 MHz), δ = 8.16 (s, 2H), 8.09 (d, 2H, J = 8.0 Hz), 7.86 (t, 1H, J = 7.6 Hz), 4.43 (t, 4H, J = 7.6 Hz), 2.00~1.92 (m, 4H), 1.45~1.36 (m, 4H),

0.98 (t, 6H, J = 7.6 Hz). ^{13}C NMR ($CDCl_3$, 100 MHz), δ = 150.0, 148.2, 137.7, 121.9, 119.1, 50.1, 32.1, 19.5, 13.3. IR (KBr) ν = 3130, 3107, 3072, 2955, 2932, 2866, 1604, 1573, 1460, 1441, 1371, 1254, 1204, 1048, 827 cm^{-1}. MS (HiResEI) Cald for $C_{17}H_{24}N_7$ (M+H) 326.2088; Found 326.2092. Anal. Calcd for $C_{17}H_{23}N_7$: C, 62.75; H, 7.12; N, 30.13. Found: C, 62.58; H, 6.90; N, 30.21.

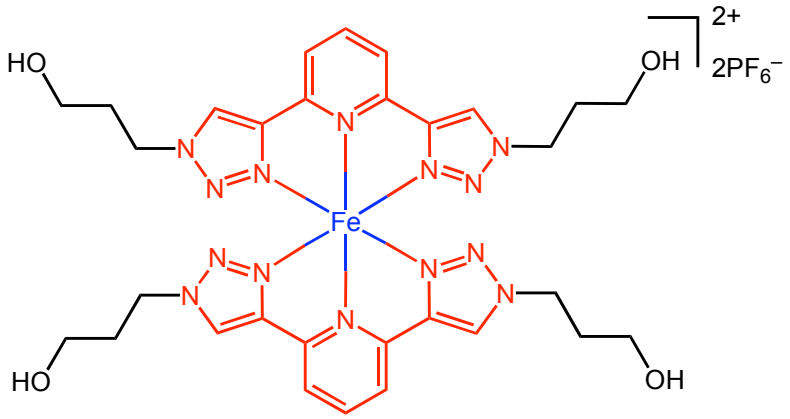

[Fe(1)$_2$]•2PF$_6$: A solution of $FeSO_4$ (0.36 mmol, 100 mg) in H_2O (100 mL) was added to a solution of **1** (0.21 mmol, 69 mg) in hot CH_3COCH_3. The solution, which immediately turned yellow-brown, was heated to 55 °C for 30 min, after which time the CH_3COCH_3 was evaporated. The iron complex was then precipitated by the addition of a saturated solution of KPF_6 (100 mL). The suspension was left for 2 h at 4 °C and the ensuing solid was filtered off, washed with H_2O, and dried under vaccum. Recrystallization by slow diffusion of ether into an MeCN solution of [Fe(**1**)$_2$]•2PF$_6$ yielded brown X-ray quality crystals (100 mg, 95% yield). ^{1}H NMR (CD_3COCD_3, 400 MHz), δ = 9.20 (s, 4H), 8.81 (d, 4H, J = 5.6 Hz), 8.56 (t, 2H, J = 7.2 Hz), 4.59~4.46 (m, 8H), 3.67 (s, br, 4H), 3.36~3.31 (m, 8H), 1.95~1.82 (m, 8H). ^{13}C NMR (CD_3CN, 75 MHz), δ = 153.7, 149.0, 140.5, 126.0, 122.5, 58.6, 50.76, 32.9. IR (KBr) ν = 3359, 3138, 2955, 2897, 1631, 1592, 1468, 1430, 1402, 1273, 1215, 1126, 1052, 846, 555 cm^{-1}. MS (HiResESI) Calcd for $C_{30}H_{38}F_6FeN_{14}O_4P$ $(M–PF_6)^+$ 859.2192, Found 859.2262. Anal Calcd for $C_{30}H_{38}F_{12}FeN_{14}O_4P_2$: C, 35.87; H, 3.81; N, 19.52. Found: C, 36.00; H, 3.99; N, 19.50.

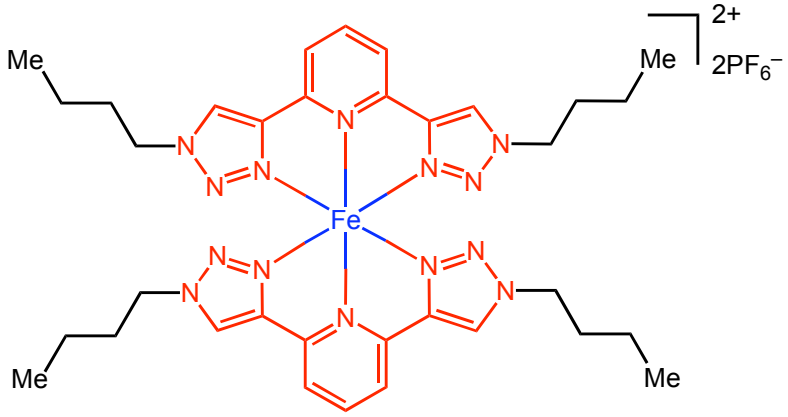

[Fe(2)$_2$]•2PF$_6$: This compound was prepared in the same manner as for [Fe(**1**)$_2$]•2PF$_6$, to produce a brown solid (94 mg, 90% yield) after isolation. ^{1}H NMR (CD_3COCD_3, 400 MHz), δ = 9.24 (s, 4H), 8.83 (d, 4H, J = 7.2Hz), 8.56 (t, 2H, J = 7.5 Hz), 4.42 (t, 8H, J = 7.2 Hz), 1.74~1.64 (m, 8H), 1.08~0.98 (m, 8H), 0.72 (t, 12H, J = 7.2 Hz). ^{13}C NMR (CD_3COCD_3, 75 MHz), δ = 154.4, 150.1, 141.5, 126.8, 124.0, 54.2, 33.4, 20.8, 14.4. IR (KBr) ν = 3146, 2959, 2939, 2874, 1631, 1592, 1464, 1433, 1348, 1270, 1211, 1134, 843, 559 cm^{-1}. MS (HiResESI) calcd for $C_{34}H_{48}F_6FeN_{14}P$ $(M\text{-}PF_6\text{+}2H)^+$ 853.3178, $C_{34}H_{46}FeN_{14}$ $(M\text{–}2PF_6)^{2+}$ 354.1763, found 853.3040, 354.1674. Anal. Calcd for $C_{34}H_{46}F_{12}FeN_{14}P_2$: C, 40.98; H, 4.65; N, 19.68. Found: C, 41.16; H, 4.83; N, 19.77.

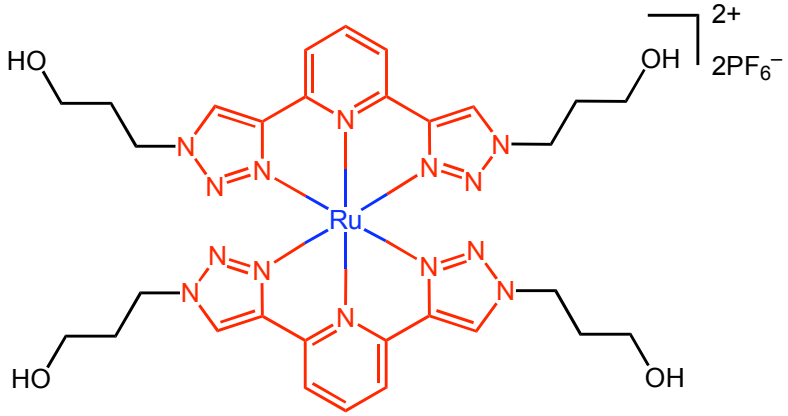

[Ru(1)$_2$]•2PF$_6$: The ligand **1** (0.21 mmol, 69 mg) in 10 mL ethylene glycol was added to the ruthenium(II) precursor $Ru(DMSO)_4Cl_2$ (0.1 mmol, 46 mg) in 4 mL 1:1 MeOH:H_2O. The mixture was heated under N_2 at 100 °C for 2.5 h, producing a yellow solution, which was then cooled to room temperature. Water was added to reach a total volume of 36 mL and solid $NH_4^+PF_6^-$ was added whereupon a yellow precipitate formed. The precipitate was washed thoroughly with H_2O and dried under vacuum. Recrystallization by slow diffusion of ether into

an MeCN solution of [Ru(**1**)$_2$]•2PF$_6$ yielded X-ray quality crystals (87 mg, 92% yield). ^{1}H NMR (CD_3COCD_3, 400 MHz), δ = 9.13 (s, 4H), 8.47 (d, 4H, J = 6.4 Hz), 8.44~8.42 (m, 2H), 4.48 (t, 8H, J = 7.2 Hz), 3.70 (t, 4H, J = 4.8 Hz), 3.39~3.36 (m, 8H), 1.94~1.90 (m, 8H). ^{13}C NMR (CD_3CN, 75 MHz), δ = 151.6, 150.2, 138.6, 126.5, 120.7, 58.6, 50.3, 32.8. IR (KBr) ν = 3414, 3138, 2944, 2878, 1623, 1584, 1460, 1430, 1402, 1344, 1266, 1208, 1127, 1052, 839, 554 cm^{-1}. MS (HiRESI) calcd for $C_{30}H_{38}F_6N_{14}O_4PRu$ 905.1894 $(M–PF_6)^+$; found 905.1953. Anal. Calcd for $C_{30}H_{38}F_{12}N_{14}O_4P_2Ru$: C, 34.33; H, 3.65; N, 18.68. Found: C, 34.42; H, 3.62; N, 18.72.

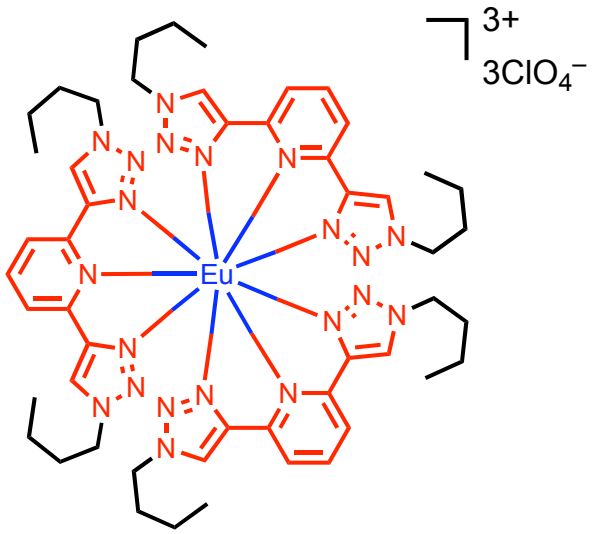

[Eu(2)$_3$]•3ClO$_4$: To a refluxing solution of **2** (0.154 mmol, 50 mg) in EtOH (3 mL) a solution of $Eu(ClO_4)_3 \cdot nH_2O$ (0.05 mol, 27.8 mg) in EtOH (2 mL) was added slowly. Reflux was maintained for 3 h, whereupon the reaction mixture was allowed to cool to room temperature to obtain a precipitate. The precipitate was filtrated and washed with cold EtOH and dried under vacuum to afford [Eu(**2**)$_3$]•3ClO$_4$ (38.5 mg, 54%). ^{1}H NMR (CD_3COCD_3, 400 MHz), δ = 7.20 (s, 6H), 6.41 (t, 3H, J = 8.0 Hz), 4.73 (d, 6H, J = 7.6 Hz), 4.71~4.64 (m, 6H), 4.51~4.40 (m, 6H), 1.80~1.64 (m, 12H), 1.10~1.04 (m, 12H), 0.85 (t, 18H, J = 7.6 Hz). ^{13}C NMR (CD_3CN, 100 MHz), δ = 160.4, 151.8, 136.8, 103.3, 88.6, 50.4, 33.8, 19.6, 13.6. IR (KBr) ν = 3107, 2955, 2928, 2874, 1619, 1588, 1569, 1464, 1250, 1203, 1095, 1029, 815, 621 cm^{-1}. MS (HiResESI) calcd for $C_{51}H_{69}ClEuN_{21}O_4$ $(M–2ClO_4)^{2+}$ 613.7364; found 613.7423. Anal. Calcd for $C_{51}H_{69}Cl_3EuN_{21}O_{12}$: C, 42.94; H, 4.88;N, 20.62. Found: C, 42.86; H, 4.67; N, 20.64.

S.2. CRYSTAL STRUCTURE ANALYSIS

The crystal structures of the Ru^{II} and Fe^{II} complexes are similar to those previously reported.[8] The crystal structure of $[Ru(\mathbf{1})_2]\bullet 2PF_6$ displays a greater degree of distortion away from the ideal octahedral geometry[8] than $[Fe(\mathbf{1})_2]\bullet 2PF_6$. Based upon the bond distances and angles around the metal center (Figure S2), the Ru^{II} complex has a local symmetry of C_1, whereas it is C_2 for the Fe^{II} complex. For Fe^{II}, the M–N_{py} bonds are equal (1.922 Å), the M–N_{tri} bond lengths are grouped into pairs at 1.948 or 1.939 Å as are the N_{tri}–Fe–N_{py} angles at 81° and 80°, and, the inter-ligand N_{py}–Fe–N_{py} is one degree away from linearity at 179°. Contrast this with the structure from Ru^{II}. In this case, all six Ru–N bonds are different lengths, although the central ones to the pyridines come close to being equivalent at 2.018(2) and 2.015(2) Å each. Admittedly there is a long and short Fe–N_{tri} bond for each of the coordinated ligands but the pair of long (2.076(2) and 2.063(2) Å) and short bonds (2.044(2) and 2.039(2) Å) do differ. However, the symmetry of the N_{tri}–Fe–N_{py} bond angles seen in the Fe^{II} complex is retained with a pair of angles at either 78° or 79°. The inter-ligand angle differs from linearity by a greater amount in the Ru^{II} complex at 175°. This distortion is believed to arise from the interplay between two types crystal-packing forces – increased steric freedom surrounding the metal-ligand environment when using triazole rings in the coordination sphere and intermolecular hydrogen bonding O–H•••O of terminal hydroxyl functionalities of the propanol arms.

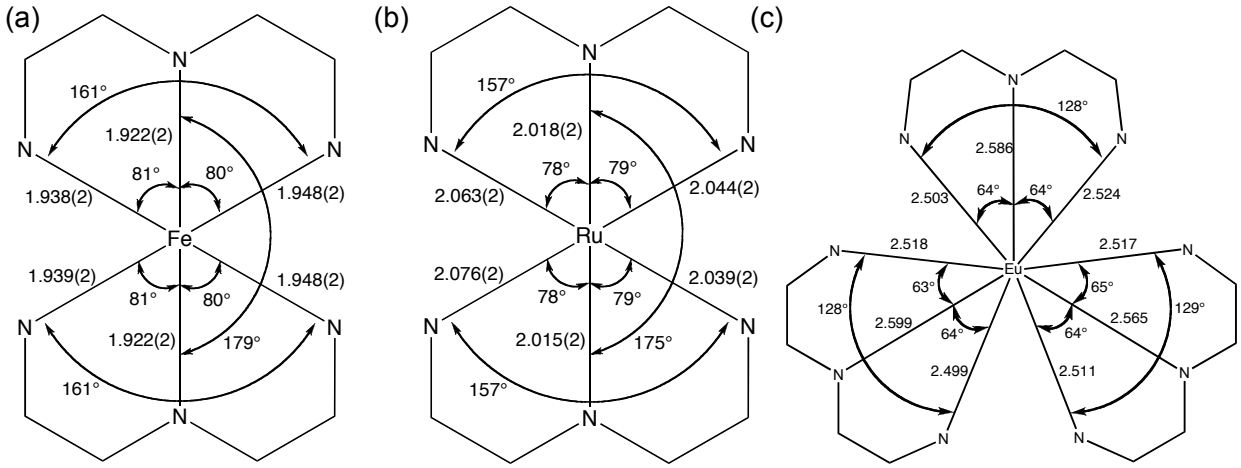

Figure S2. Distances and angles within the coordination environment of (a) $[Fe(\mathbf{1})_2]\bullet 2PF_6$, (b) $[Ru(\mathbf{1})_2]\bullet 2PF_6$ and (c) $[Eu(\mathbf{2})_3]\bullet 3ClO_4$.

Intermolecular π-π stacking is also present in similar degrees for the Ru^{II} and Fe^{II} crystal structures. The π-π stacking is observed between the central pyridine ring systems ~3.3 Å on adjacent pairs of complexes (Figure S3) in the form of ring-over-bond overlap. The open sterics provided by the triazole N2' nitrogens plays a role here by allowing for the close approach of the H4 proton of the pyridine to the neighboring molecule thereby facilitating the chance for ideal π overlap.

In the case of Ru^{II}, the expanded metal ion, $d(Ru–N_{py})$ = 2.051 Å; $d(Fe–N_{py})$ = 1.922 Å, increases the space and therefore capacity for distortion about the metal center. When this feature is coupled with the presence of hydrogen bonding, a more distorted octahedral geometry is observed. In the crystal structure of $[Ru(\mathbf{1})_2]•2PF_6$, every hydroxyl group participates in an *infinite* chain[9] (Figure S3) that passes from one end of the crystal to the other. This hydrogen bonding results from σ-bond cooperativity in which the O–H•••O bond angles are close to linear thereby defining directional two-center bonds.[10] Inspecting the alternative long-short $Ru–N_{tri}$ bond lengths, a few observations are worth noting. The two short bonds are both located on the triazole rings wherein the hydroxyl of the attached propanol arms are bonded to each other via a hydroxyl bridge provided by an adjacent molecule in the crystal structure. Of the two long bonds, one of them connects to the hydroxyl that serves as the aforementioned bridge for a different neighboring molecule. The final long bond extends to a hydroxyl group that serves to inter-molecular bridge between the hydroxyl units of two other molecules. The crystal structure of $[Fe(\mathbf{1})_2]•2PF_6$ also displays a hydrogen bond network that involves a disordered H_2O molecule and PF_6^- anion.

When all these features are considered together, the reduced steric constraints provided by the N2' nitrogen together with the expanded Ru^{II} ion both facilitate greater distortion from octahedral symmetry arising from the extensive hydrogen bonding throughout the crystal. This finding reinforces the impact that the two triazole ring systems incorporated into the tripy ligand structures have on the resulting solid-state structures.

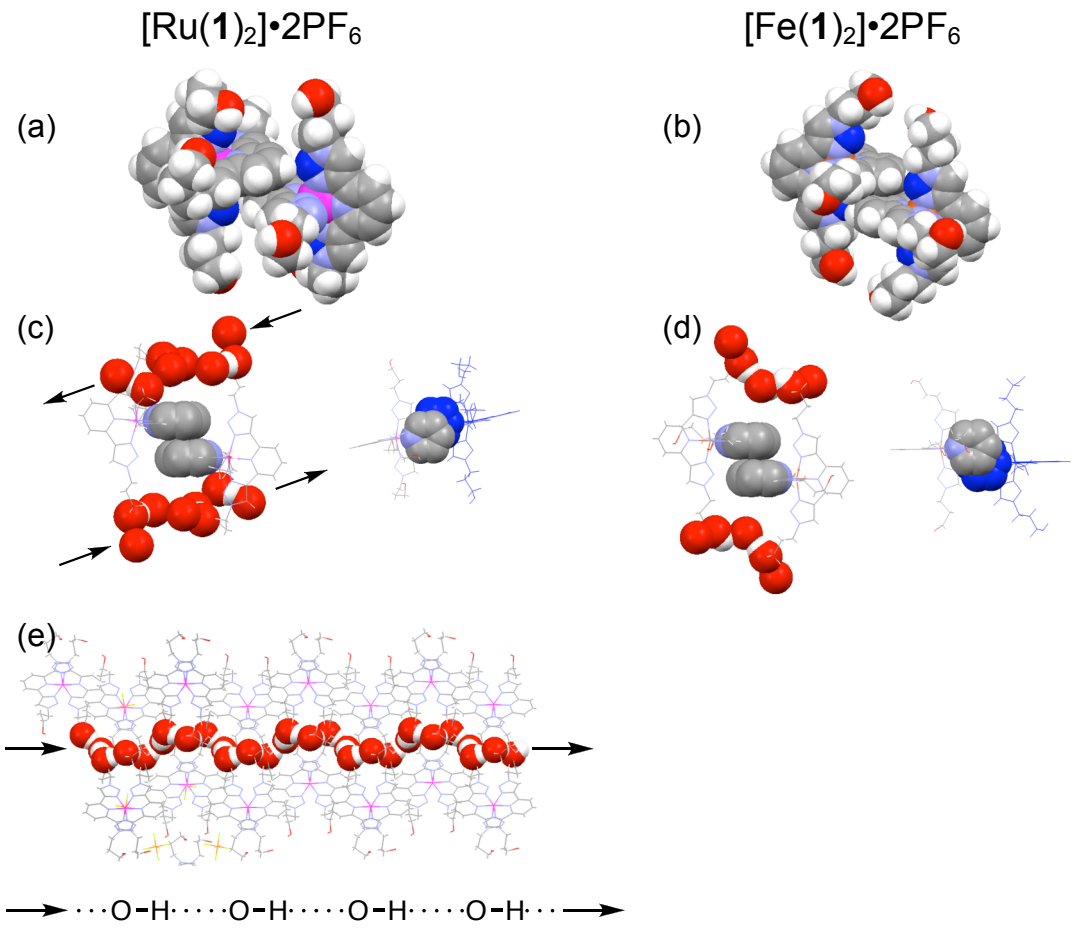

Figure S3. Representations of dimers present in the (a) $[Ru(\mathbf{1})_2]\bullet 2PF_6$ and (b) $[Fe(\mathbf{1})_2]\bullet 2PF_6$ crystal structures highlighting the N2' nitrogen of the triazole rings (dark blue) and its effect on intermolecular π-π stacking; representations of dimers of (c) $[Ru(\mathbf{1})_2]\bullet 2PF_6$ and (d) $[Fe(\mathbf{1})_2]\bullet 2PF_6$ show the combination of π-π stacking and hydrogen bonding; extended representation of (e) $[Ru(\mathbf{1})_2]\bullet 2PF_6$ highlighting the infinite chain of directional two center hydrogen bonds that runs throughout the entire crystal (space-filling, O–H•••O angles spread from 154° to 174° and O•••O distances average at 2.819 Å).

S.3. ^{1}H NMR SPECTROSCOPY

The ^{1}H NMR spectroscopy was recorded to investigate the effect of coordination on ligand proton resonances. In all cases, the H5' proton of the triazole units is the most downfield of the ligands **1** and **2** (Figures S4 and S5) and of the complexes, followed by the H3,5 and H4 protons

on the pyridine ring. For the $[Fe(\mathbf{1})_2]\bullet 2PF_6$, $[Ru(\mathbf{1})_2]\bullet 2PF_6$ and $[Fe(\mathbf{2})_2]\bullet 2PF_6$ complexes (Figures S6, S7 and S8), the H5', H3,5 and H4 resonances all shift downfield by about 0.6 ppm, and this is attributed to the induced charge, π-cloud perturbation and the conformational changes that occur as a consequence of coordination. Furthermore, the –OH hydroxyl protons are observed in the spectra of the ligand **2** as a singlet at ~3.9 ppm and also for the complexes $[Fe(\mathbf{1})_2]\bullet 2PF_6$ and $[Fe(\mathbf{1})_2]\bullet 2PF_6$, modestly shifted upfield by ~0.1 ppm. In each case, the integrated intensity is ~75% of what it should be, presumably due to ^{2}D exchange with solvent.

The ^{1}H NMR spectrum of $[Eu(\mathbf{2})_3]^{3+}$ (Figure S9), displays one set of peaks consistent with one dominant species in solution. The H3,5 protons on the pyridine display the greatest lanthanide induced shift (LIS) of ~3.2 ppm upfield, whereas, the pyridine H4 proton and the triazole H5' protons shift upfield by ~1.5 ppm. The protons on the butyl chain in the methyl, H3" and H2" positions display modest shifts, whereas the H1" proton is split evenly into two 1:1 multiplet resonances labeled $H1"_A$ and $H1"_B$ at 4.66 and 4.45 ppm, respectively. In the case of $H1"_A$, the resonance is close to that for the H3,5 protons. This splitting is not observed for **1** or **2**, neither for $[Fe(\mathbf{1})_2]^{2+}$, $[Fe(\mathbf{2})_2]^{2+}$ nor $[Ru(\mathbf{1})_2]^{2+}$. The crystal structure for this compound shows that five of the six methylene units corresponding to H1" protons are oriented in the same way. For this major conformation, the H1" protons are either directed towards or away from the Eu^{III} center. This observation implies that a through-space LIS distinguishes between both H1" protons and that the two proton environments are exchanging slowly on the ^{1}H NMR timescale.

The presence of just one form of $[Eu(\mathbf{2})_3]^{3+}$ in solution is in stark contrast with the analogous $[Eu(terpy)_3]^{3+}$ complex in CD_3CN, which exists in three different forms that are best described[11] by a stability ordering with respect to the coordination number: 8-coordinate > 9-coordinate >> 7-coordinate. This difference to the tris-terpy complex arises from the exchange of the terminal pyridine units in terpy for the triazole rings in tripy. This replacement effectively removes the C–*H* protons α to the coordinating nitrogen on the terminal pyridine units and consequently, removes their destabilizing steric interaction with an adjacent terpy ligand. This interaction is readily seen in the distortion[8] of $[Eu(terpy)_3]^{3+}$ from D_3 symmetry to C_2 and the resulting nonplanarity of the terpy ligands to alleviate the C–*H* proton-to-ligand steric clash.

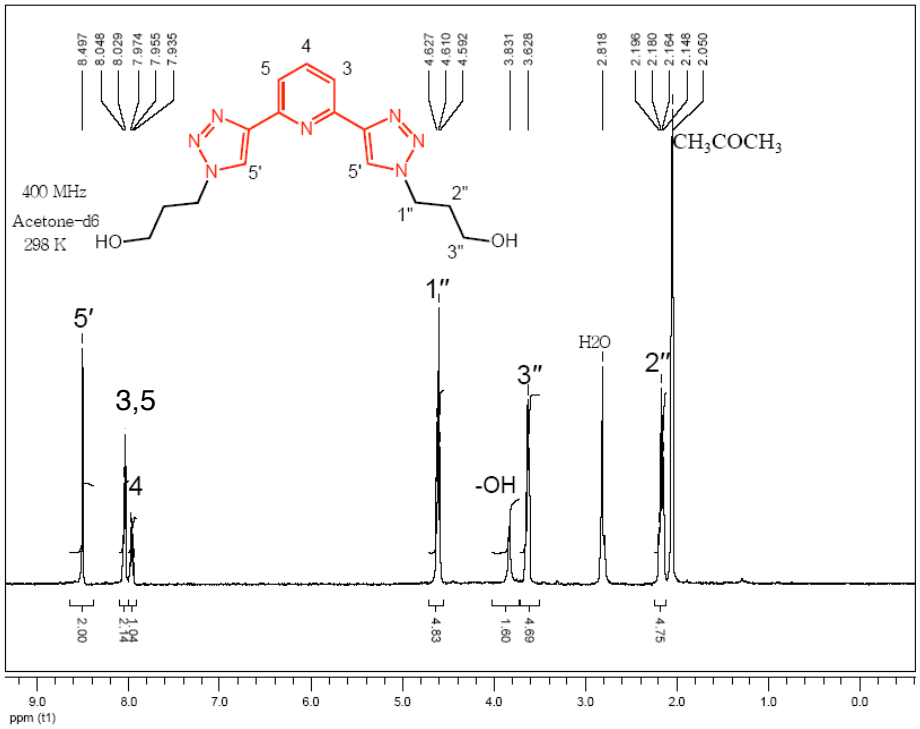

Figure S4. Full ^{1}H NMR spectrum (400 MHz, CD_3COCD_3) of **1**.

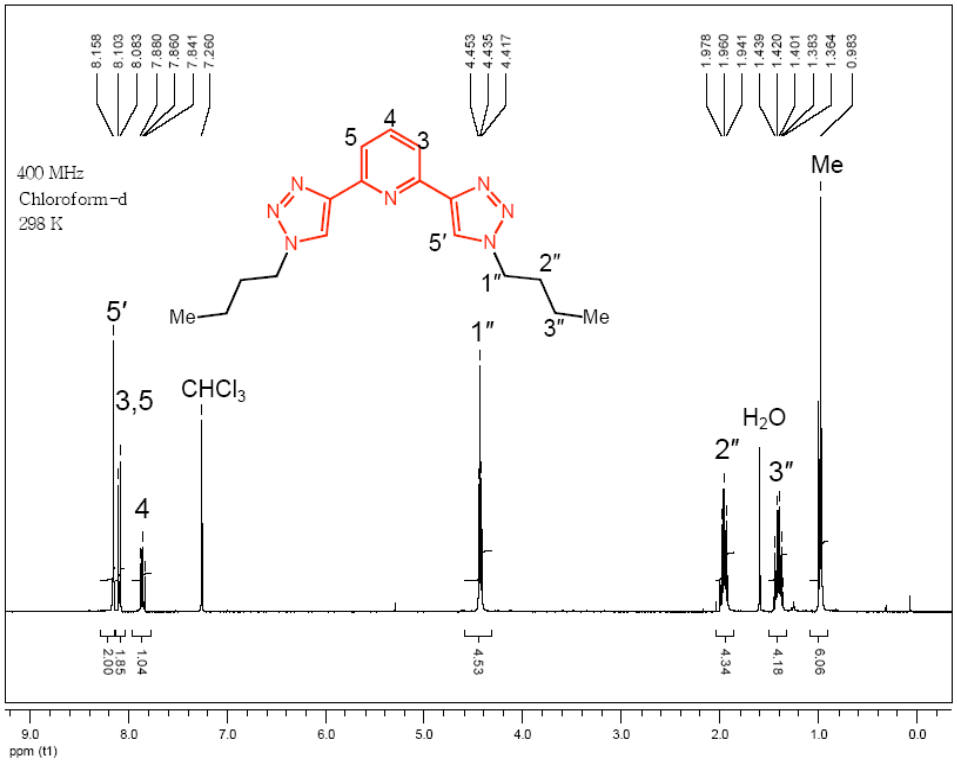

Figure S5. Full ^{1}H NMR spectrum (400 MHz, $CDCl_3$) of **2**.

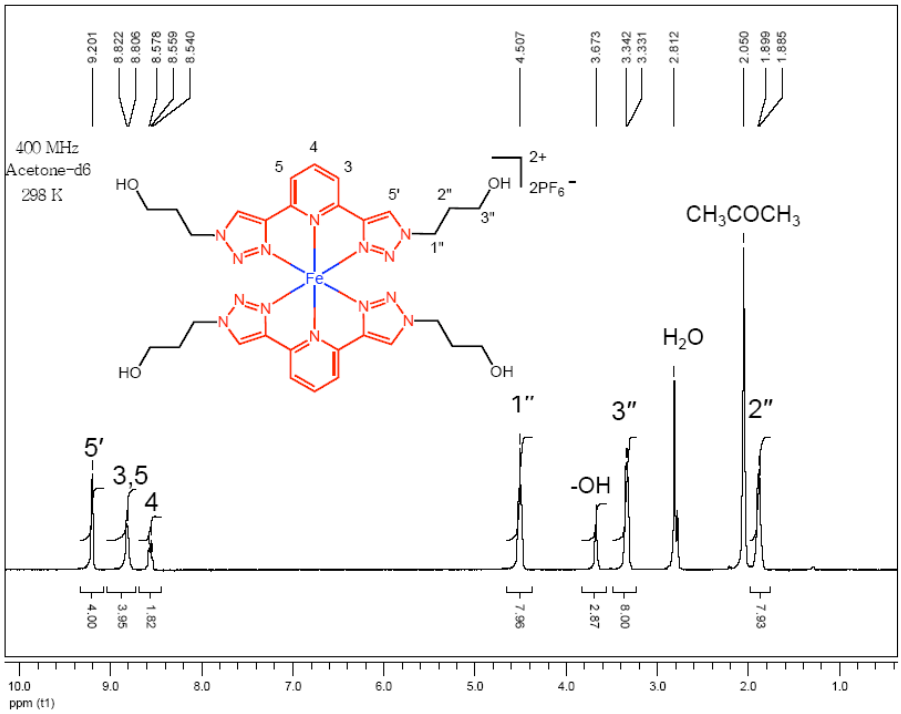

Figure S6. Full ^{1}H NMR spectrum (400 MHz, CD_3COCD_3) of $[Fe(\mathbf{1})]^{2+}$.

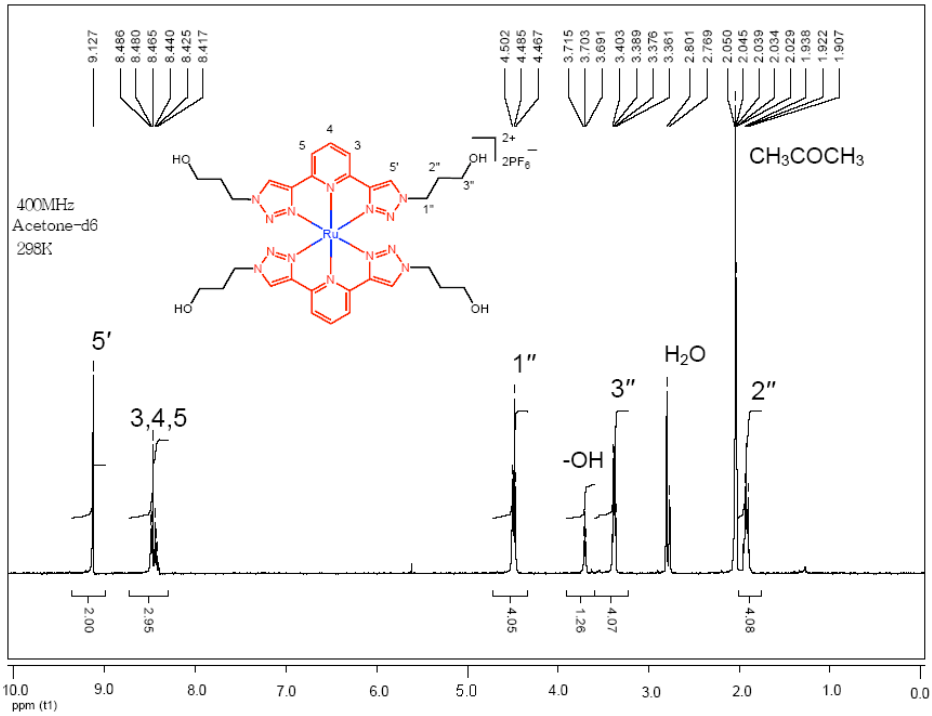

Figure S7. Full ^{1}H NMR spectrum (400 MHz, CD_3COCD_3) of $[Ru(\mathbf{1})_2]^{2+}$.

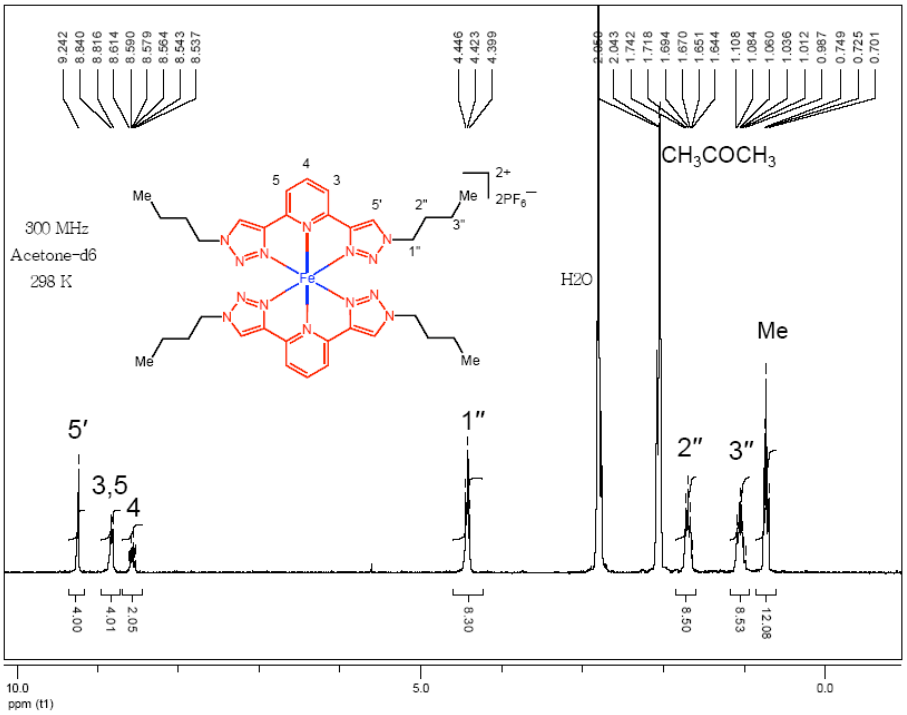

Figure S8. Full ^{1}H NMR spectrum (300 MHz, CD_3COCD_3) of $[Fe(\mathbf{2})_2]^{2+}$.

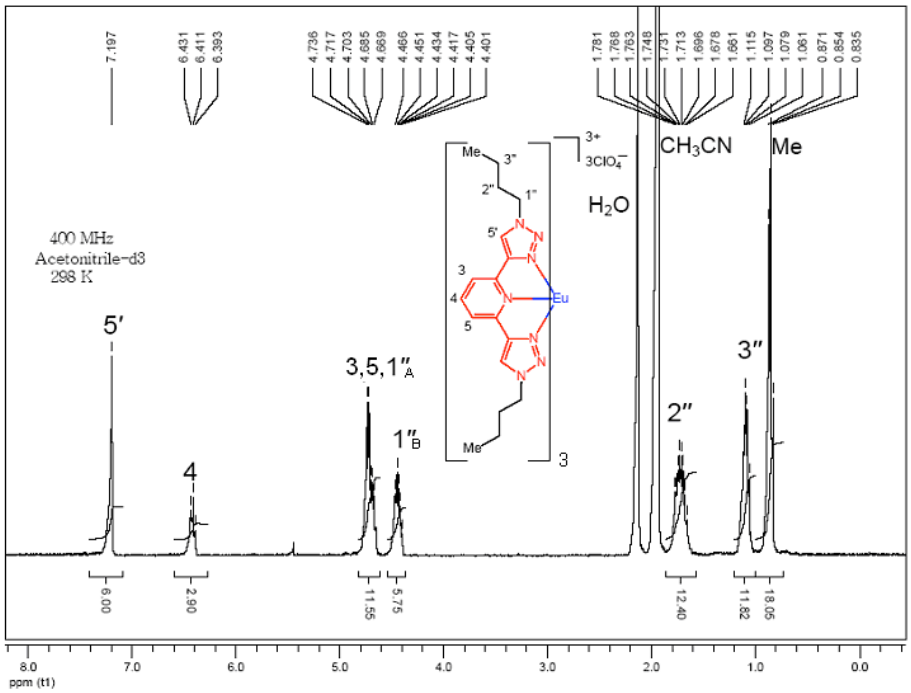

Figure S9. Full ^{1}H NMR spectrum (400 MHz, CD_3CN) of $[Eu(\mathbf{2})_3]^{3+}$.

S.4. MOLECULAR MODELING OF THE SOFTENED GEOMETRICAL CONSTRAINTS FOR THE TRIPY CORE MOTIF IN AN OCTAHEDRAL FIELD

In order to provide more insight into the role that the sterically open N2' nitrogens of the triazole rings play in octahedral iron complexes, a simple molecular model was investigated. The energy associated with deformation around the Fe center was calculated by constraining the inter-ligand angle θ (Figure S14a) between the central Fe–N(pyridine) bond of one ligand and the Fe–N(triazole) of the other ligand. The energy was calculated for both bis-tripy and bis-terpy complexes based on tripy and terpy core structures. The counterions of both complexes were omitted and the terminal propanol arms branching out from the tripy core were replaced with methyl groups. For the tripy and terpy complexes, the minimized structures (SPARTAN minimizer) displayed inter-ligand angles of θ = 111.9 and 105.5°, respectively. This 6° difference reflects the geometrical difference between the 5- or 6-membered ring systems of the terminal triazole or pyridine moieties for tripy or terpy, respectively. Constraints were placed on the inter-ligand angle and the energy minimized subsequently to generate plots (Figure S14b) of deformation energy versus the change in the angular coordinate. The angular coordinate was determined as the relative angle of deformation between the optimized geometry and the constrained one: 111.9° – θ and 105.5° – θ for tripy and terpy, respectively. These plots indicate that the use of tripy core effectively halves the energy arising from deformation of the inter-ligand angle when compared with terpy.

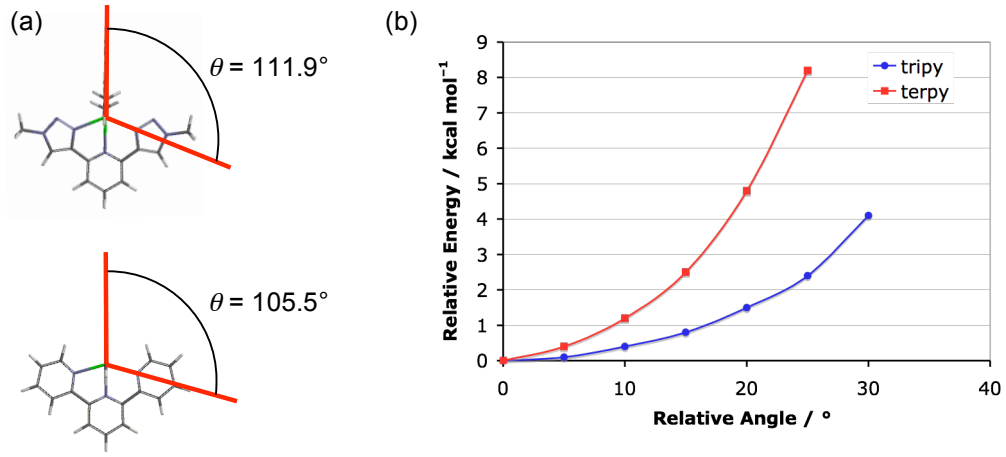

Figure S10. Definition of the inter-ligand angle θ for a model bis-tripy and bis-terpy iron complex, which is constrained to estimate by (b) the relative deformation energy (SPARTAN minimizer) as a function of relative angle (= 111.9° – θ for tripy and = 105.5° – θ for terpy)

S.5. ELECTROCHEMISTRY

A survey of the electrochemistry of the Fe^{II}, Ru^{II} and Eu^{III} complexes were performed in order to compare and contrast their properties with the terpy complexes. During the course of the CV experiments on $[Fe(\mathbf{1})_2]^{2+}$ (Figure S11), a sensitivity to H_2O was observed (Figure S12) following on from inserting the SCE into the solution. Subsequently, the reversible oxidation process at +1.2 V changes to display a scan-rate dependent quasi-reversible behavior. By contrast, addition of H_2O by means of the SCE has no influence on the CV behavior of $[Fe(terpy)_2]^{2+}$ and $[Ru(\mathbf{1})_2]^{2+}$ complexes (Figure S13a,b). To investigate this relationship further, the methylated version of **1** was used to prepare the complex, $[Fe(\mathbf{2})_2]\bullet 2PF_6$ confirming that the Fe^{III} redox product was not related (Figure S13c) to a coordination mode involving the hydroxyl end groups. Secondly, known amounts of H_2O were added to the CV solution of $[Fe(\mathbf{2})_2]^{2+}$ with the concomitant increase in the degree of quasi-reversible behavior (Figure S14). A full discussion of this behavior is presented in the next **Section S.6**.

The quasi-reversible two-electron reduction of $[Ru(\mathbf{1})_2]^{2+}$ (Figure S15) assigned to a ligand-localized process was investigated as a function of scan rate. As the scan rate increases, the reduction peak at –1.7 V increases peak intensity and shifts to more negative potentials. However, there are two features in the return sweep that indicate that the product of reduction is formed at rates faster than those determined by the 500 mV s^{-1} scan rate, i.e., faster than 3 s^{-1}. The corresponding oxidation peak begins to emerge as a broad signal at –1.2 V and the oxidation of the reduction product shifts to more negative potentials from +0.6 to +0.4 V. It was found that consecutive CV cycles were identical.

For $[Eu(\mathbf{2})_3]^{3+}$, the CV shows (Figure S16) quasi reversible behaviour for the reduction of Eu^{III} (–0.66 V). In the anodic region, the first oxidation wave, assigned to the coordinated ligand **2**, is highly irreversible. For this reaon, only the peak potentials for the forward scans are reported in Table S2. The difference in potential between the $Eu^{III/II}$ reduction and oxidation of **2** is comparable to those found for the triple helical complexes with terpy.[12]

The CV of the free ligand, **2**, (Figure S17) displays an irreversible reduction at –2.5 V and oxidation at +1.9 V. Upon coordination to Fe^{II}, the reduction is stabilized by ~800 mV. The same can be said for coordination to Ru^{II} even although the reduction is quasi-reversible. This observation is consistent with the stabilization of the ligand LUMO due to coordination to the electropositive metal centers.

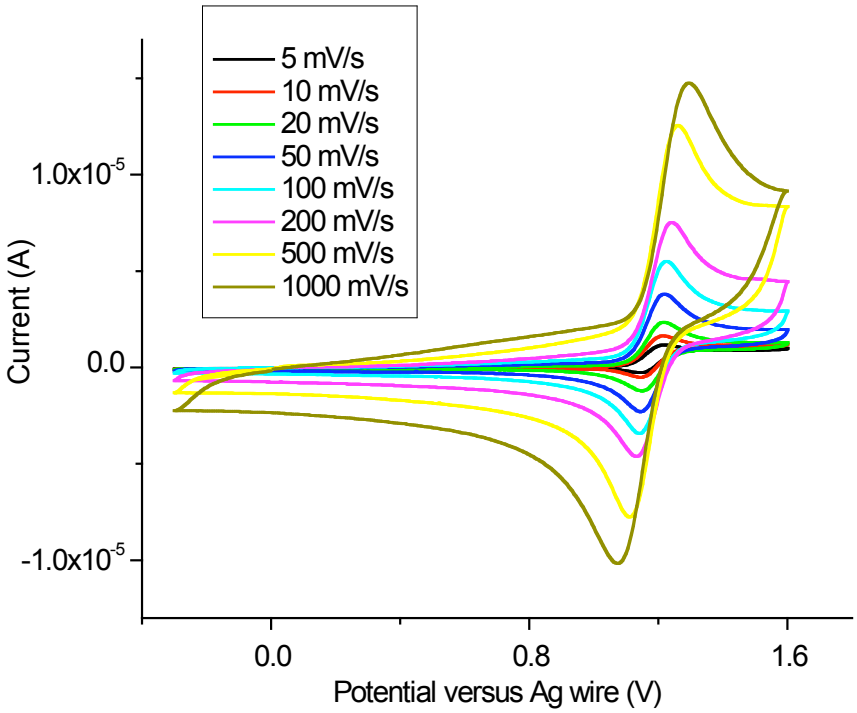

Figure S11. CV for $[Fe(\mathbf{1})_2]^{2+}$ at different scan rates (1.4 mM, MeCN, 0.1 M $TBAPF_6$).

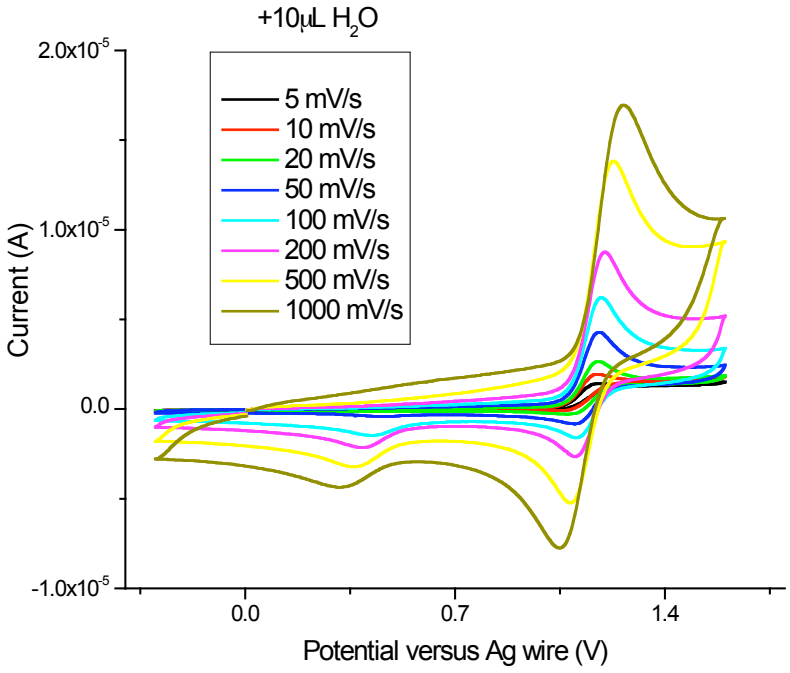

Figure S12. CV of $[Fe(\mathbf{1})_2]^{2+}$ in the presence of 10 μL of H_2O at different scan rates (1.2 mM, MeCN, 0.1 M $TBAPF_6$).

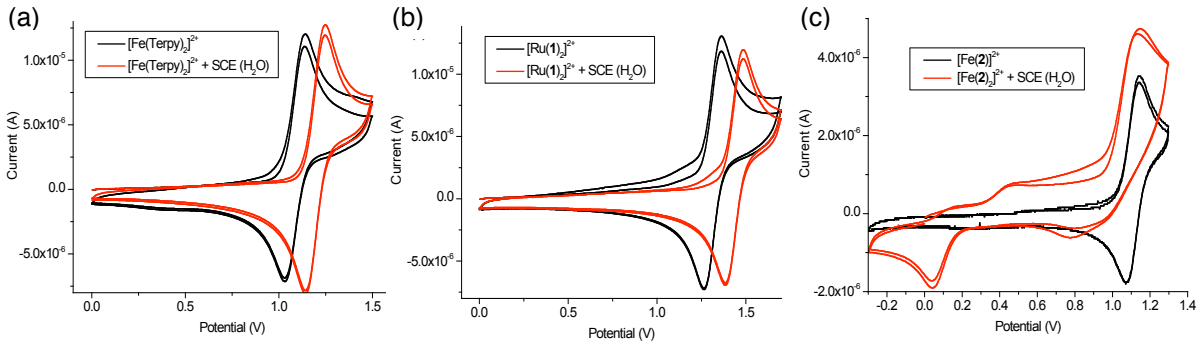

Figure S13. CV (ν = 200 mV s^{-1}) of $[Fe(\mathbf{2})_2]^{2+}$, $[Fe(terpy)_2]^{2+}$ and $[Ru(\mathbf{1})_2]^{2+}$ after the addition of H_2O in the form of the SCE reference electrode (MeCN, 0.1 M $TBAPF_6$). Black trace: Ag wire reference electrode; red trace: SCE reference electrode.

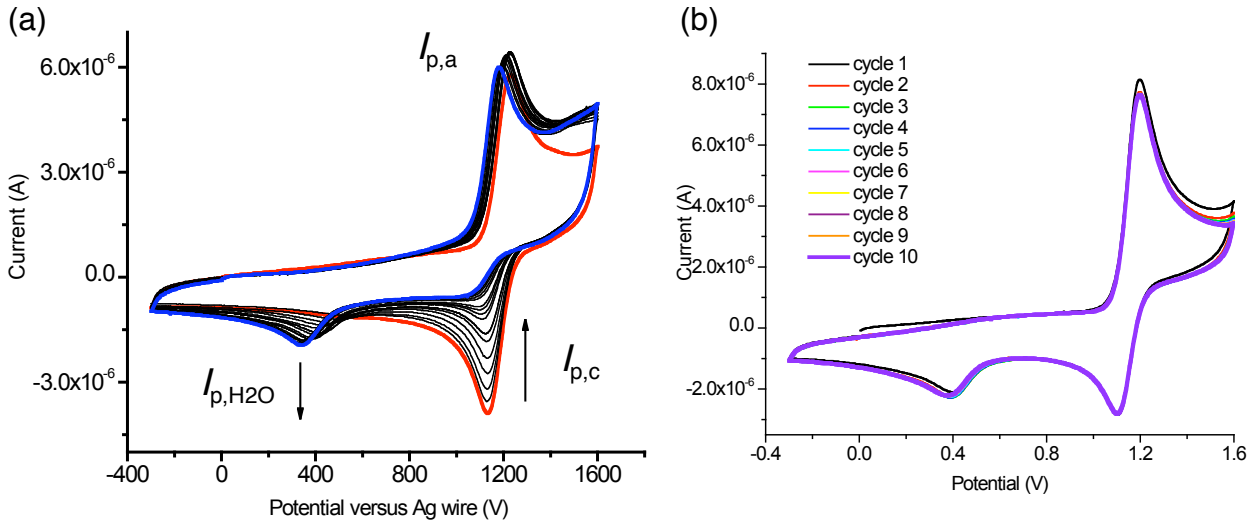

Figure S14. (a) CV of $[Fe(\mathbf{1})_2]^{2+}$ (ν = 200 mV s^{-1}, 1.3 mmol) in anhydrous MeCN (red trace) and upon the addition of 1, 2, 3, 4, 5, 6, 7, 8, 9, 10, 11, 14, 16, 18, 20, 22, 25 (blue trace) μL of H_2O (MeCN, 0.1 M $TBAPF_6$). (b) CV of $[Fe(\mathbf{1})_2]^{2+}$ (ν = 200 mV s^{-1}, 1.3 mmol) with 10 μL of H_2O (MeCN, 0.1 M $TBAPF_6$), during 10 consecutive cycles.

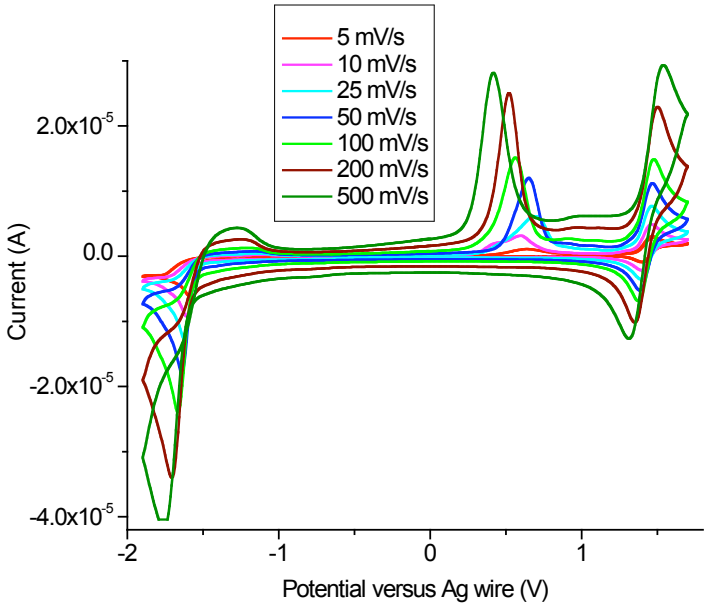

Figure S15. CV of $[Ru(\mathbf{1})_2]^{2+}$ at different scan rates (1.3 mM, MeCN, 0.1 M $TBAPF_6$).

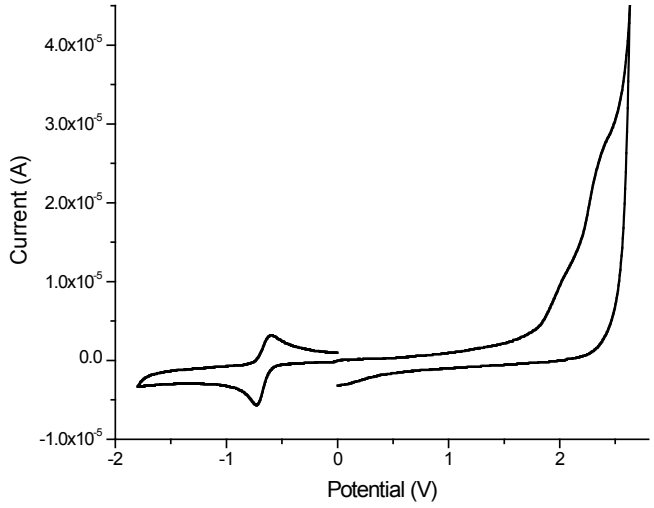

Figure S16. CV of $[Eu(\mathbf{2})_3]^{3+}$ (ν = 200 mV s^{-1}, 1.1 mM, MeCN, 0.1 M $TBAPF_6$). Ag wire as reference electrode and corrected to SCE electrode.

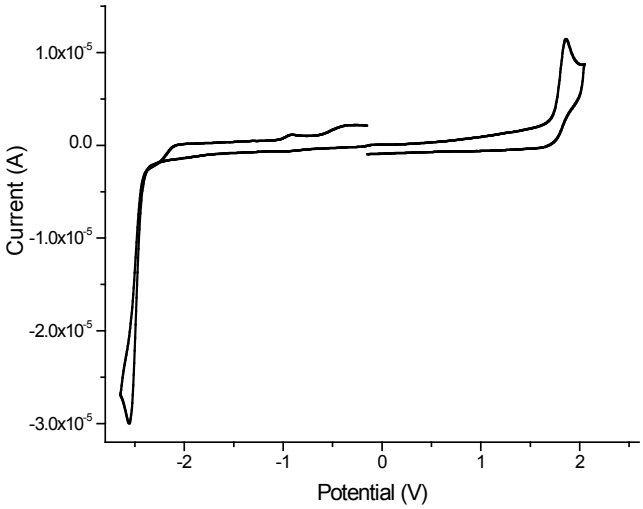

Figure S17. CV of **2** (200 mV s^{-1}, 1.5 mM, MeCN, 0.1 M $TBAPF_6$). Ag wire as reference electrode and corrected to SCE electrode.

Table S2. Comparison of CV and UV-Vis Spectroscopic Data[a]

	$E_{1/2}$(Ox) V	$E_{1/2}$(Red1) V	$E_{1/2}$(Red2) V	λ_{max} (ε_{max})[c] nm (× 10^5 M^{-1} cm^{-1})	ΔE(redox)[d] V	E_{MLCT} eV[e]
	Metal	Ligand	Ligand			
$[Fe(terpy)_2]^{2+}$	1.09	–1.27	–1.43	552 (1.76), 319 (7.65)	2.36	2.25
$[Fe(\mathbf{1})_2]^{2+}$	1.03	–1.53	–1.83	442 (1.23), 295 (4.68)	2.56	2.81
$[Ru(terpy)_2]^{2+}$	1.26	–1.28	–1.54	475 (1.83), 308 (7.79)	2.54	2.61
$[Ru(\mathbf{1})_2]^{2+}$	1.32	–1.8[b]		394 (1.50), 284 (5.48)	3.10	3.15
2	1.9[b]	–2.55		301 (1.32)		
	Ligand	Metal				
$[Eu(\mathbf{2})_3]^{3+}$	2.0[b], 2.4[b]	–0.66		309 (3.87)		

[a] Potentials versus SCE, ν = 200 mV s^{-1}, MeCN, 0.1 M $TBAPF_6$) [b] peak potential value used from irreversible process [c] MeCN [d] $\Delta E(\text{redox}) = E_{1/2}(\text{Ox}) - E_{1/2}(\text{Red1})$ [e] $E_{MLCT} = ((10^7\ \text{nm}\cdot\text{cm}^{-1}) / \lambda) / 8065\ \text{cm}^{-1}\cdot\text{eV}^{-1}$

S.6. CHARACTERIZATION OF REDOX-STIMULATED AQUATION OF $[Fe(\mathbf{1})_2]^{3+}$ USING ELECTROCHEMISTRY

The CV data of $[Fe(\mathbf{1})_2]^{2+}$ upon the addition of H_2O (Figure S14) were analyzed based on a model of aquation of the Fe^{III} redox center that can be reversed upon reduction to the Fe^{II} center (Scheme S1) consistent with an EC mechanism. The peak current of the redox waves assigned to each species in solution has been measured as a function of the addition of increasing amounts of H_2O: Oxidation of $[Fe(\mathbf{1})_2]^{2+}$ leads to peak current $I_{p,a}$; reduction of any residual $[Fe(\mathbf{1})_2]^{3+}$ $I_{p,c}$; and reduction of the aquation product $[Fe(\mathbf{1})(\mathbf{1}\text{–}N)(OH_2)]^{3+}$ $I_{p,H2O}$. Based on the concentration of $[Fe(\mathbf{1})_2]^{2+}$ (1.3 mM), this spans the addition of 0 to 1.25 equivalents of H_2O.

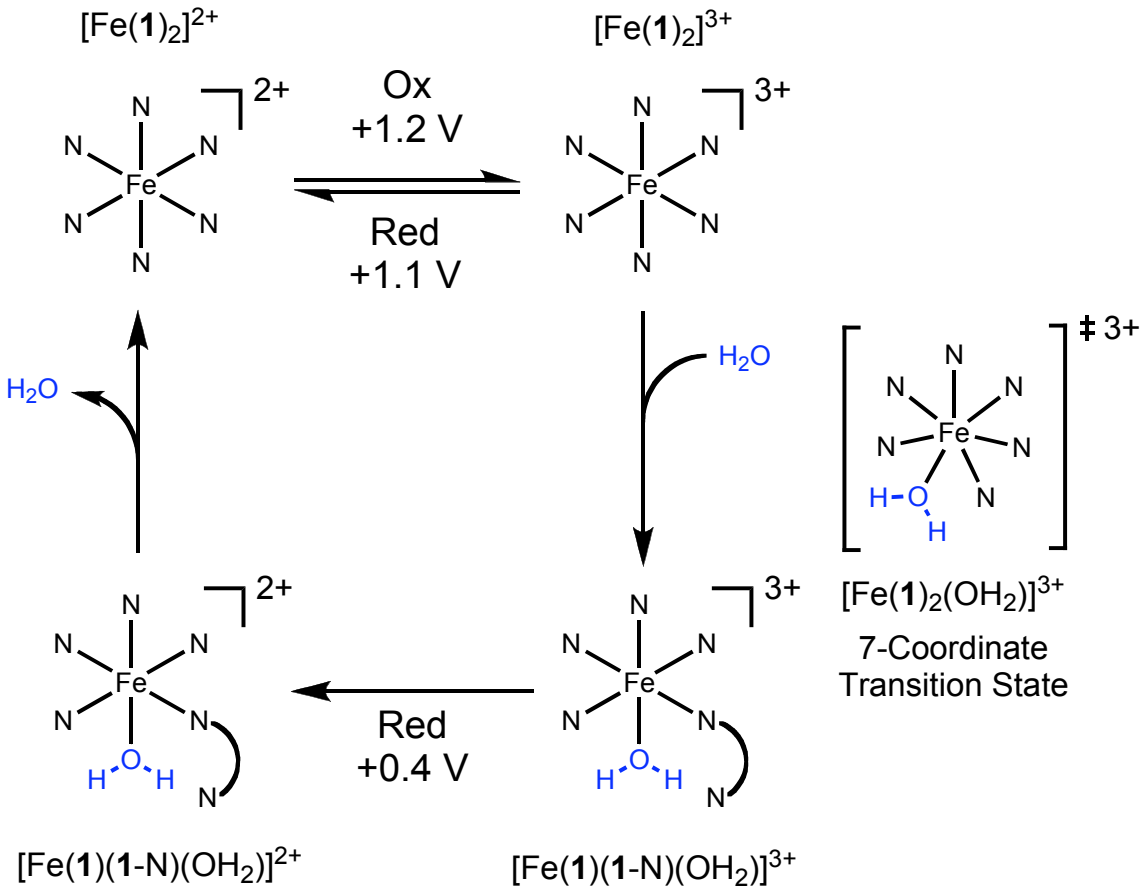

Scheme S1. Proposed scheme for the reversible redox-stimulated aquation of $[Fe(\mathbf{1})_2]^{2+}$ that goes via a 7-coordinate transition state.

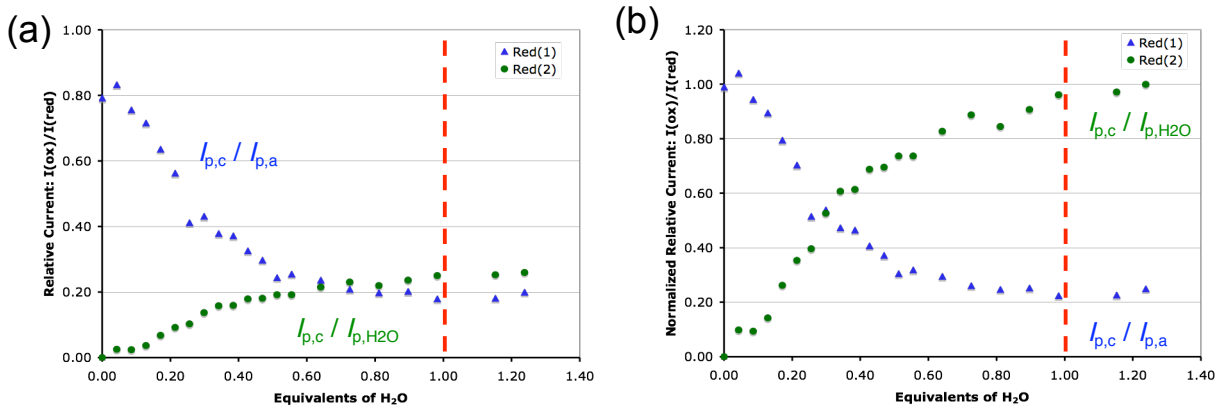

Figure S18. Plots of (a) peak current ratios and (b) normalized peak current ratios versus the equivalents of H_2O added into the solution of $[Fe(\mathbf{1})_2]^{2+}$.

From the current ratio plots, the decrease in the Fe^{III} parent reduction peak ($I_{p,c}$) at +1.1 V correlates with the increase in the aquation product's reduction peak ($I_{p,H2O}$) at +0.4 V. The peak current ratios (Figure S18a) and related normalized current ratios (Figure S18b) of both reduction processes compared to the oxidation, i.e., $I_{p,c}$ / $I_{p,a}$ and $I_{p,H2O}$ / $I_{p,a}$, suggest 1:1 binding between H_2O and the electrogenerated Fe^{III} redox state $[Fe(\mathbf{1})_2]^{3+}$. However, the peak current is only 25% of the value expected assuming there is 100% conversion to the aquation product after addition of 1 equivalent of H_2O. Changing the scan rate (Table S3) did not influence the current peak ratios for either reduction process in a systematic manner. Inspection of the second consecutive CV cycle, for any of the scan rates probed (5 – 1000 mV s^{-1}), shows that it is coincident with the first cycle. This observation alone provides compelling evidence that the *entire* process is fully reversible and that the lower than expected current values for the cathodic peak at +0.4 is associated with either (1) a slower rate of heterogeneous electron transfer, or (2) smaller diffusion constant for the Fe^{III} aquation product, than for $[Fe(\mathbf{1})_2]^{3+}$. The CV data (Table S3) suggest a product is formed faster than the time between oxidation to the Fe^{III} state and its reduction at +1.1 V.

Table S3. Peak current ratios for reduction processes compared to the primary oxidation in anhydrous MeCN and with the addition of H_2O[a]

	Anhydrous MeCN	+10 μL H_2O	
Scan rate / mV s^{-1}	$I_{p,c}$ / $I_{p,a}$	$I_{p,c}$ / $I_{p,a}$	$I_{p,H2O}$ / $I_{p,a}$
5	0.98	0.88	[b]
10	0.98	0.81	[b]
20	0.95	0.66	0.02
50	0.91	0.51	0.07
100	0.89	0.44	0.32
200	0.84	0.49	0.30
500	0.99	0.56	0.22
1000	0.85	0.62	0.17
2000	-	0.54	0.13

[a] All data obtained from CV studies (0.1 M $TBAPF_6$, Ag wire pseudo reference electrode) for anhydrous MeCN (sample ~ 1.4 mM) and with 10 mL of H_2O (sample ~ 1.2 mM). b No peak intensity was observed for these scan rates.

Information about the aquated product can be inferred from an examination of the CVs, a survey of the known crystal structures of related compounds as a measure of prevalence for certain coordination motifs as well as the shallow potential energy surface for deformation of the inter-ligand angle, θ about the Fe center (**Section S.4.**). Comparison of the CVs of $[Fe(\mathbf{1})_2]^{2+}$ and $[Ru(\mathbf{1})_2]^{2+}$, show that only the iron complex displayed a facile susceptibility to H_2O. This observation correlates well with the presence of more than 12 *aquated* and *hepta*coordinate Fe^{II} or Fe^{III} complexes[13] and the paucity of any form of heptacoordinate Ru^{III} complexes. For the iron complexes, most of them incorporate multidentate ligands, for example, the hexadentate ethylenediaminetetraacetate tetraanion (EDTA), incorporating both N and O atom donors. These crystal structures show a H_2O molecule coordinated in a reasonably open looking pocket provided by the other ligand(s). By contrast, seven-coordinate complexes of ruthenium, in any oxidation state, occur with hydrides or unsaturated ligands,[14] even although the hexacoordinate monoaquated Ru^{II} complexes can be made routinely.[15] This literature survey correlates well with the susceptibility of the $[Fe(\mathbf{1})_2]^{3+/2+}$ oxidation towards H_2O. This information suggests that the electrogenerated Fe^{III} center can accommodate H_2O in a seventh coordination site when there is sufficient room to do so, either transiently, or as a stable compound. This pathway is blocked for

the $[Fe(terpy)_2]^{2+}$ complex with the steric protection provided by the proximal C–*H* proton. This pathway is likely to be rarer for Ru complexes, presumably on account of electronic factors rather than steric ones.

Regarding the nature of the aquated product, the electrochemistry and some molecular modeling (SPARTAN minimizer) helps to provide insight into the electronic and steric environment surrounding the Fe^{III} center, respectively. These is a significant 800 mV shift between the reduction of the Fe^{III} parent complex $[Fe(\mathbf{1})_2]^{3+}$ at +1.1 V and the aquation product +0.4 V. This shift can be related to smaller shifts in the same direction observed for 6-coordinate environments between compounds with and without one N-donor ligand replaced for H_2O. For example, the oxidation couple for $[Ru(bpy)_3]^{3+/2+}$ is 1.02 V vs SCE,[16] whereas the related complex, $[Ru(bpy)_2(py)(OH_2)]^{3+/2+}$ is at 0.78 V vs SCE[15a] (bpy = 2,2'-bipyridine; py = pyridine) consistent with a stabilization of 240 mV; similarly, the oxidation of *trans*-$[RuCl(cyclam)(py)]^{2+/+}$ is at +0.32 vs NHE, whereas for *trans*-$[RuCl(OH_2)(cyclam)]^{2+/+}$ it lies at 0.012 V vs NHE (cyclam = 1,4,8,11-tetraazacyclotetradecane) relating into a stabilization of 310 mV.[17] These examples are consistent with the results obtained here that, the replacement of an N-donor ligand by H_2O stabilizes the $Fe^{III/II}$ redox potential. The magnitude of the shift for $[Fe(\mathbf{1})_2]^{3+/2+}$ is, however, significantly larger. This ~500 mV discrepancy suggests that a 7-coordinate species with its additional N-donor atom might be the aquation product.

To investigate the viability of a 7-coordinate bis-tripy complex of iron, a molecular mechanics study was conducted and the results compared to the bis-terpy analog. For this purpose, monoaquated 7-coordinate bis-tripy and bis-terpy Fe complexes were constructed and their geometries optimized (Figure S19). In order to accommodate the single H_2O molecule, the inter-ligand angle, θ, in tripy was found to decrease from ~112° to ~86° and for terpy from ~106° to ~97° corresponding to a reduction of 26° and 9°, respectively. Even although this coordinate is not the sole one responsible for minimizing the molecular mechanics energy in this simulation, its large change in the tripy complex suggests that a greater amount of the geometrical requirements for aquation can be mediated by a reduction in the inter-ligand angle for the complexes with tripy than for terpy.

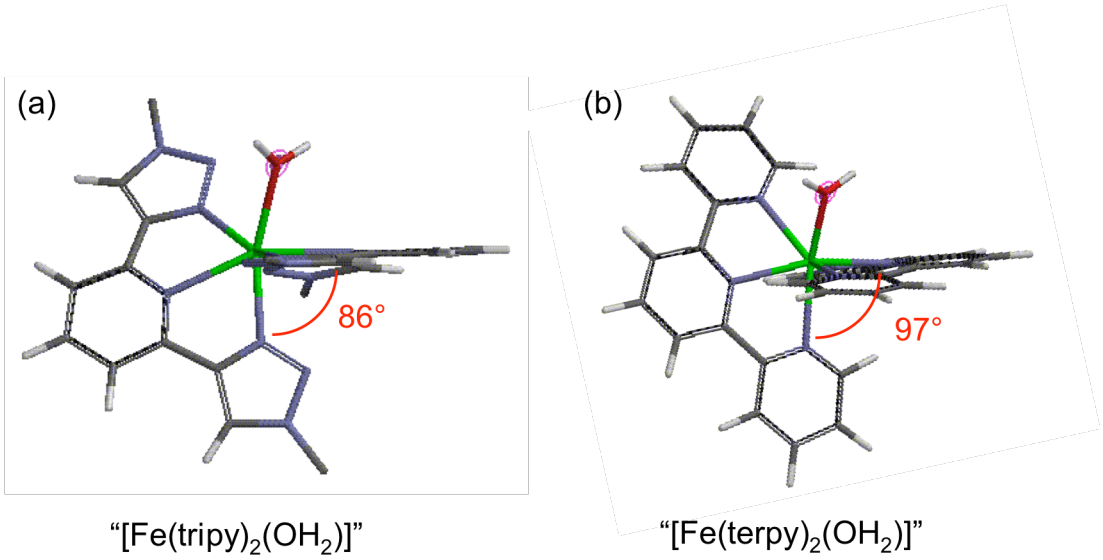

Figure S19. Geometry optimized structures (SPARTAN minimizer) of model 7-coordinate iron complexes of tripy and terpy.

In summary, the influence of H_2O on the CV of $[Fe(\mathbf{1})_2]^{2+}$ is attributed to a molecular event involving the coordination of H_2O to either produce a not uncommon 7-coordinate Fe^{III} complex, $[Fe(\mathbf{1})_2(OH_2)]^{3+}$, or to go through a heptaocoordinate species heading to a 6-coordinate product, $[Fe(\mathbf{1})(\mathbf{1}–N)(OH_2)]^{3+}$. This effect, therefore, is facilitated by the more exposed iron center when the more open triazole ring systems are employed.

S.7. EMISSION SPECTROSCOPY

In MeCN solution, ligands **1** and **2** are fluorescent (Figure S20), the complex $[Eu(\mathbf{2})_3]^{3+}$ displays mixed emission[12b] (Figures S21 and S22) in the form of phosphorescence from the Eu^{III} center and fluorescence from **2**, whereas none of the Fe^{II} or Ru^{II} complexes displayed any emission properties in the conditions investigated. Both ligands display the same emission (λ_{max} = 337 nm) and excitation (λ_{max} = 300 and 238 nm) maxima consistent with the same emissive core. The emissive state is sensitized at the same wavelengths of maximum of absorption of the ligand (Figure S23). The phosphorescence of the Eu^{III} center displays two characteristic and sharp bands at 592 and 616 nm that display maximum excitation at 274 and 337 nm. In addition, the relative contribution of fluorescence from the ligand **2** to the emission spectra of $[Eu(\mathbf{2})_3]^{3+}$ increases

compared to Eu^{III} phosphorescence with dilution from 200 to 50 μM, consistent with ligand disassociation at these concentrations.

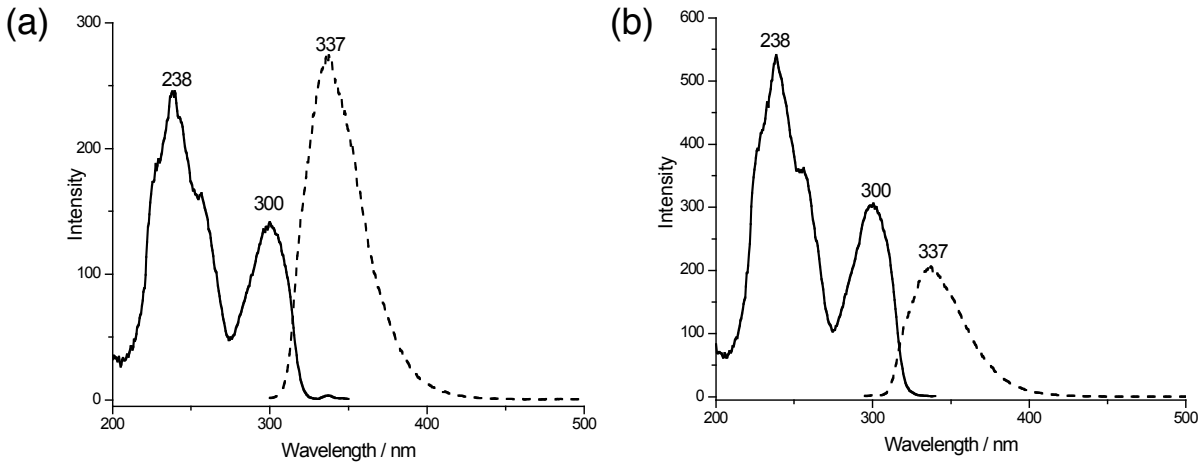

Figure S20. Emission (dashed line) and excitation (solid line) spectra of (a) **1** (4.86 μM, CH_3CN, λ_{exc} = 375 nm, λ_{em} = 280 nm) and (b) **2** (4.31 μM, CH_3CN, λ_{exc} = 360 nm, λ_{em} = 275 nm).

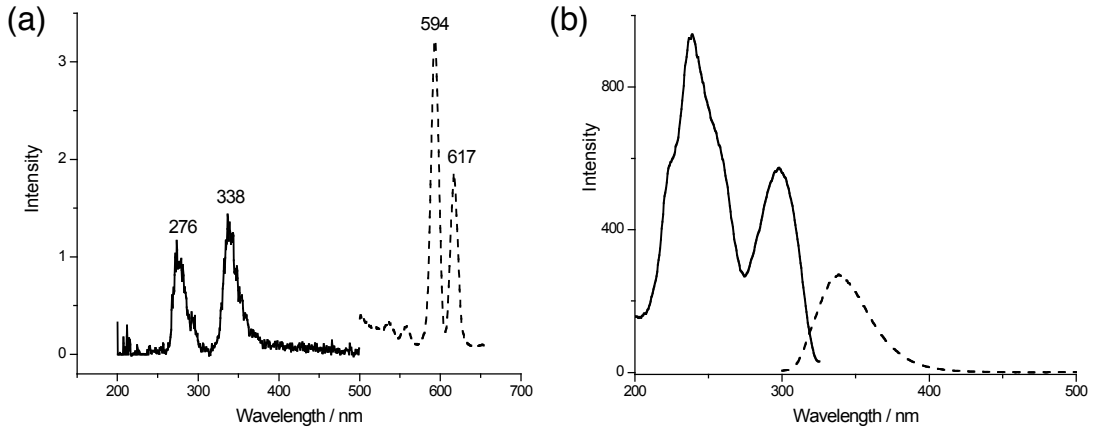

Figure S21. Emission (dashed line) and excitation (solid line) spectra of $[Eu(\mathbf{2})_3]^{3+}$ in CH_3CN. (a) The phosphorescence from the Eu^{III} center (211 μM, λ_{exc} = 338 nm, λ_{em} = 594 nm) and (b) fluorescence from **2** (4.21 μM, λ_{exc} = 274 nm, λ_{em} = 340 nm) can both be observed.

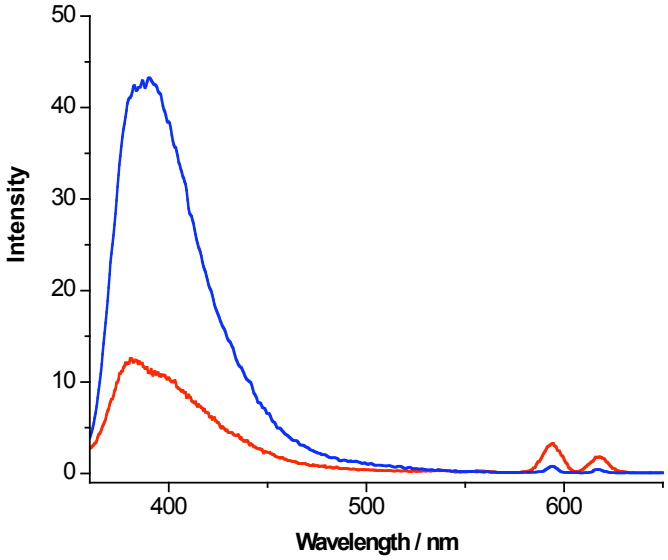

Figure S22. Emission spectra of $[Eu(\mathbf{2})_3]^{3+}$ in MeCN at room temperature with excitation at 338 nm at 200 (red) and 50 μM (blue).

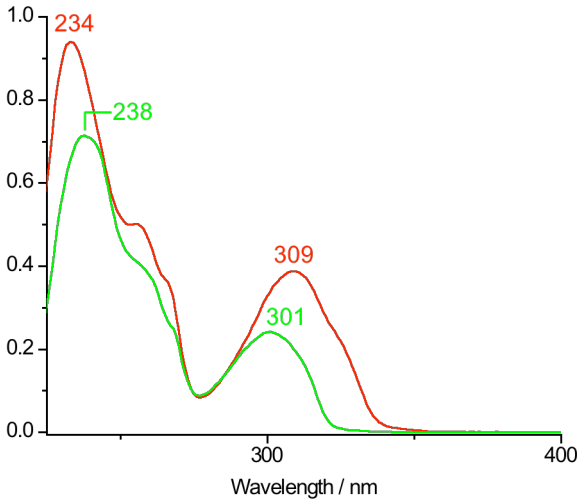

Figure S23. UV-Vis spectra of **2** and $[Eu(\mathbf{2})_3]^{3+}$ in MeCN.

S.8. ^{13}C NMR AND MASS SPECTRA

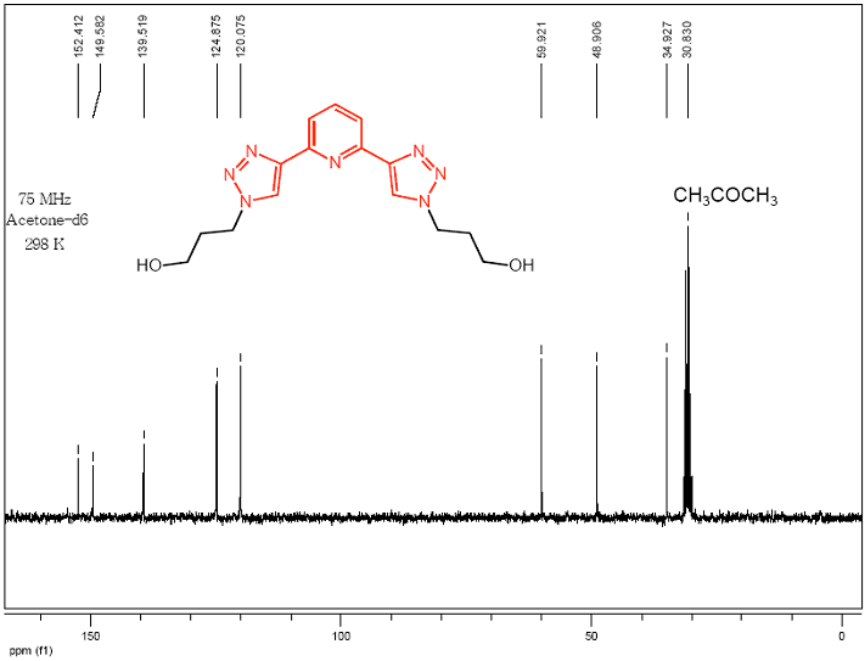

Figure S24. Full ^{13}C NMR spectrum (75 MHz, CD_3COCD_3) of **1**.

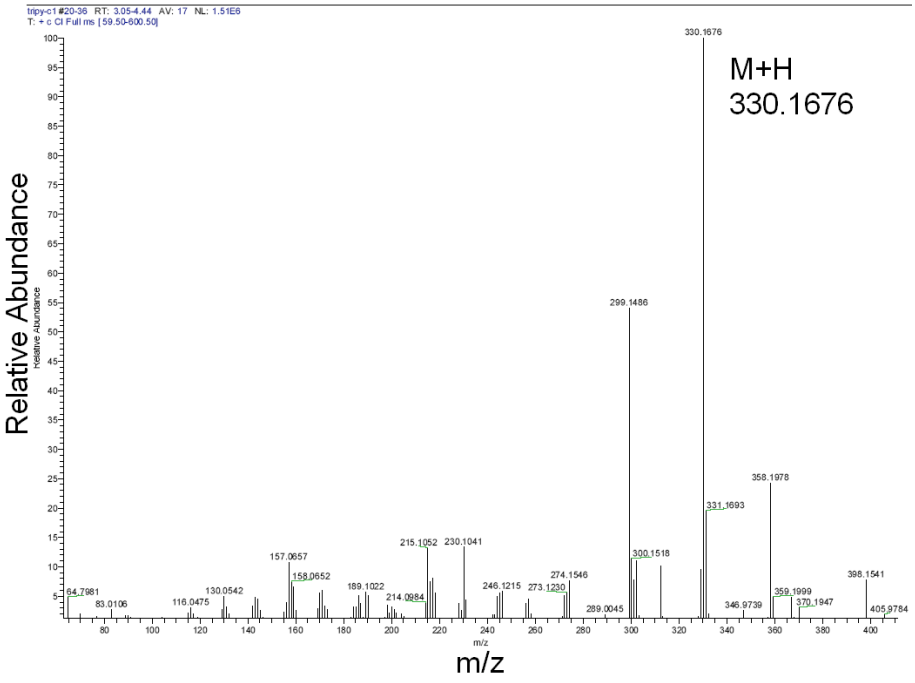

Figure S25. HiRes EI spectrum of **1**.

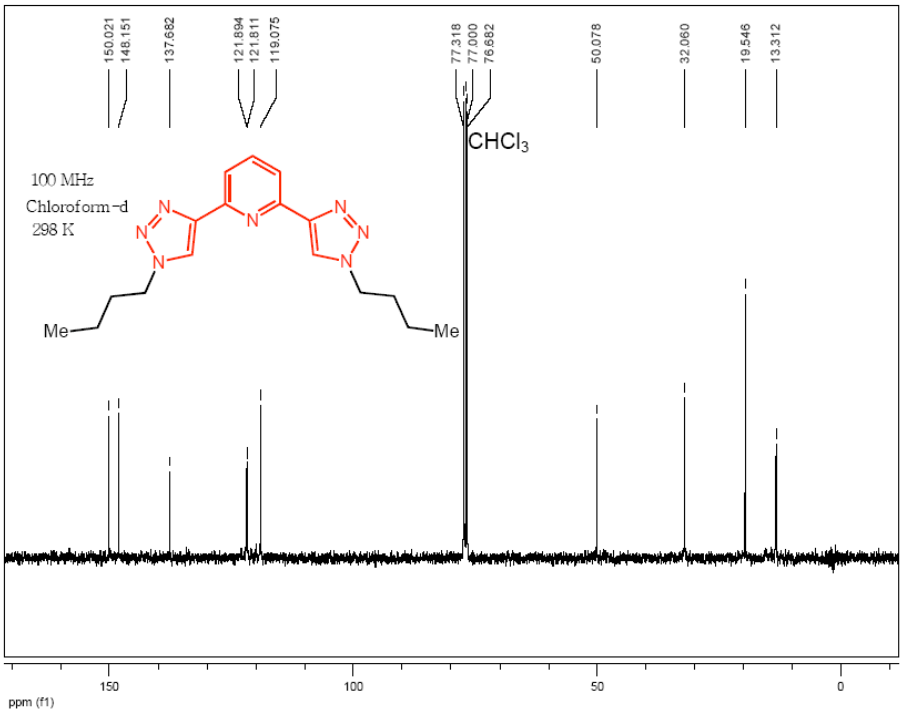

Figure S26. Full ^{13}C NMR spectrum (100 MHz, $CDCl_3$) of **2**.

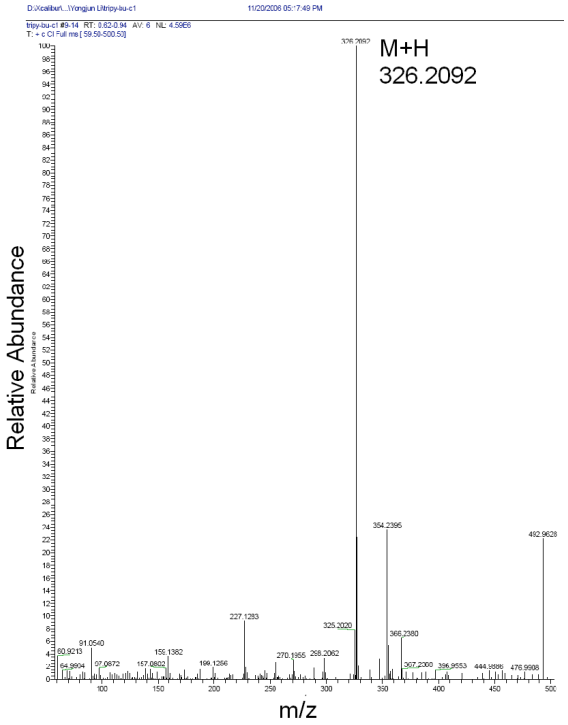

Figure S27. HiRes EI spectrum of **2**.

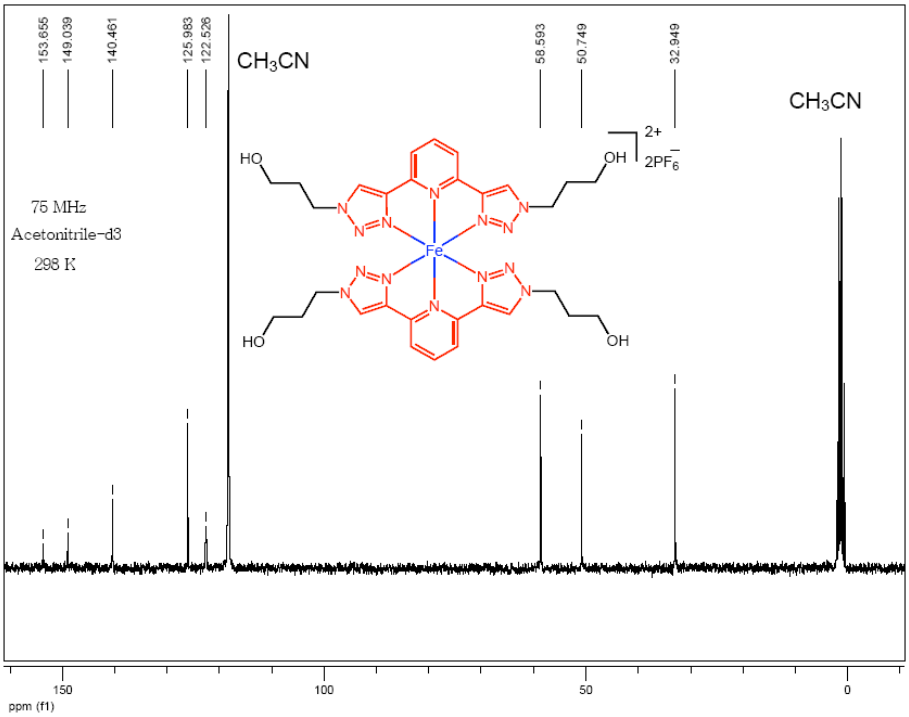

Figure S28. Full ^{13}C NMR spectrum (75 MHz, CD_3CN) of $[Fe(\mathbf{1})_2]^{2+}$.

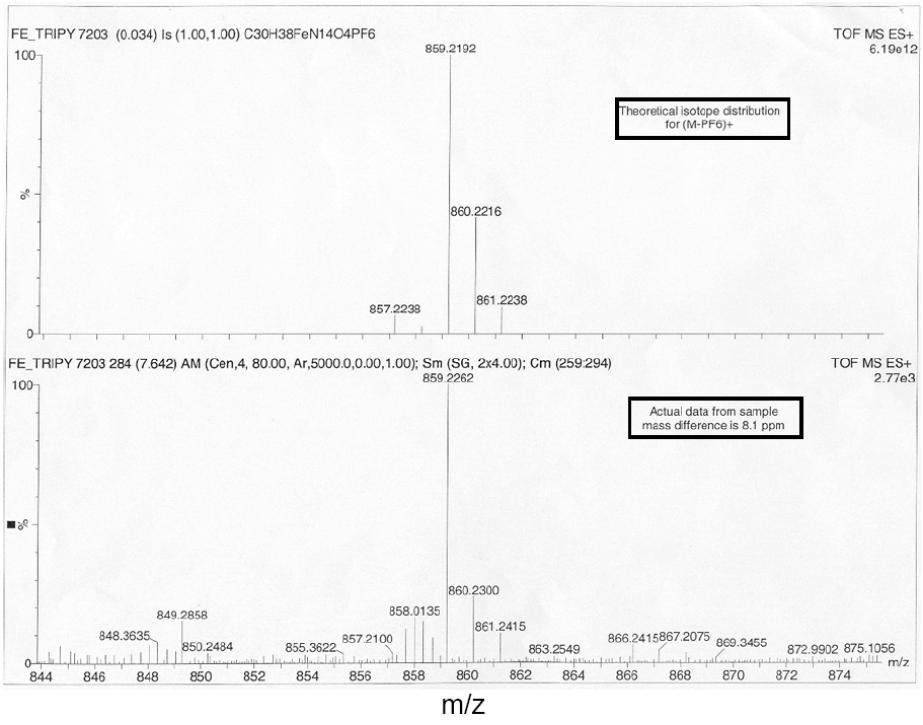

Figure S29. HiRes ESI spectrum of $[Fe(\mathbf{1})_2]\bullet 2PF_6$.

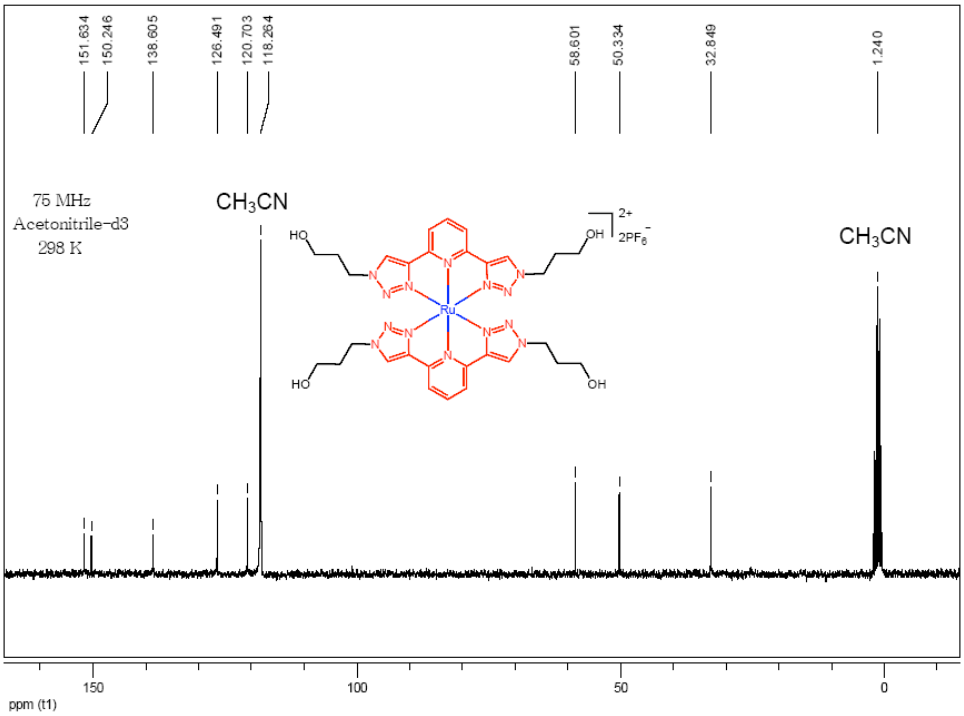

Figure S30. Full ^{13}C NMR spectrum (75 MHz, CD_3CN) of $[Ru(\mathbf{1})_2]^{2+}$.

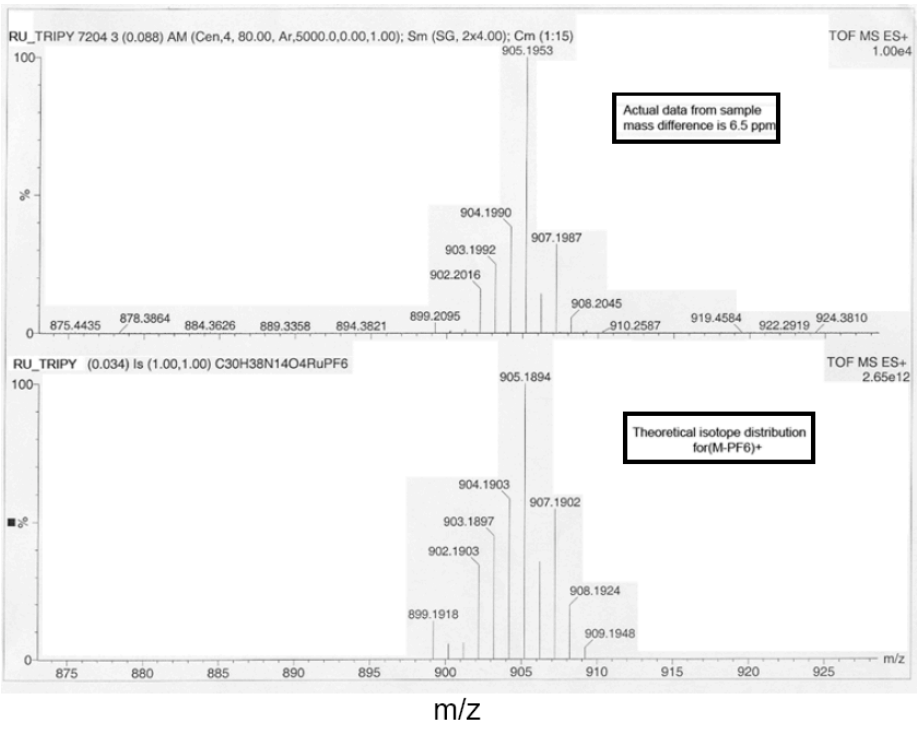

m/z

Figure S31. HiRes ESI spectrum of $[Ru(\mathbf{1})_2]\bullet 2PF_6$.

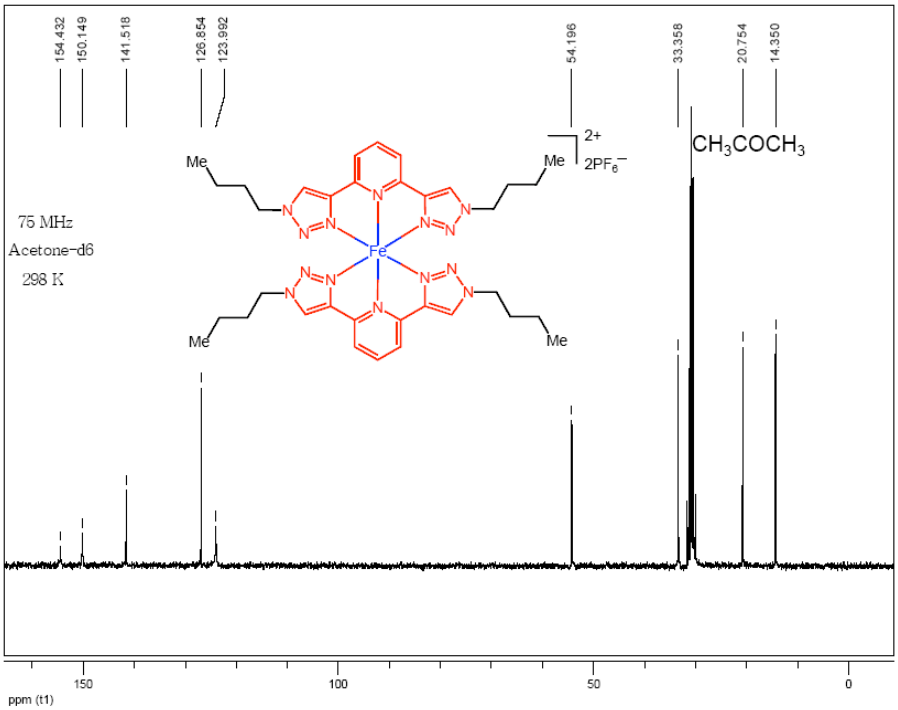

Figure S32. Full ^{13}C NMR spectrum (75 MHz, CD_3COCD_3) of $[Fe(\mathbf{2})_2]^{2+}$.

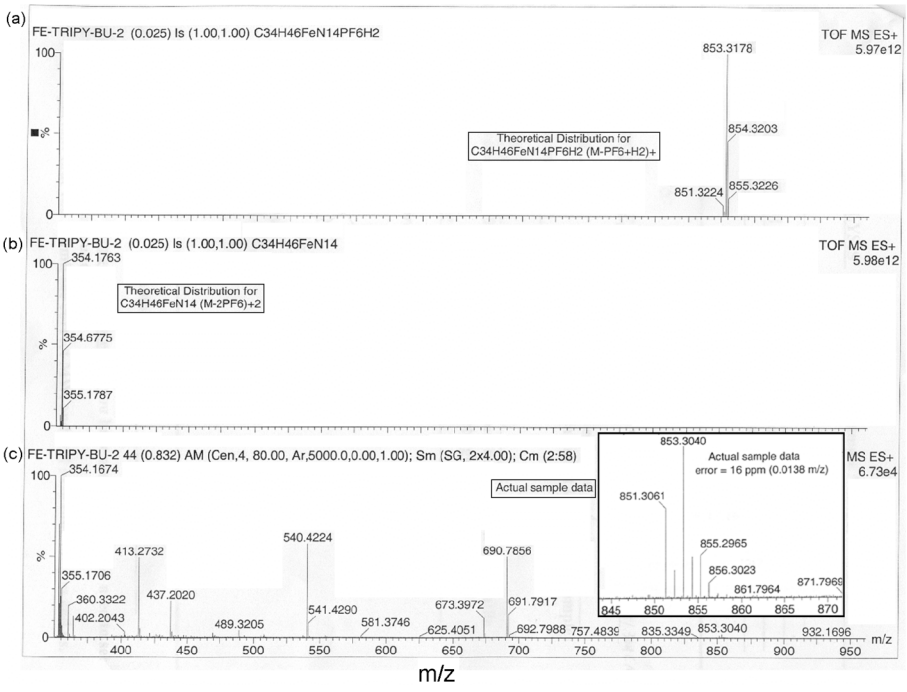

Figure S33. Theoretical HiRes ESI spectra of (a) the $(M–PF_6+H_2)^+$ ion and (b) the $(M–2PF_6)^{+2}$ ion that are both observed in (c) the actual sample data of $[Fe(\mathbf{2})_2]\bullet 2PF_6$.

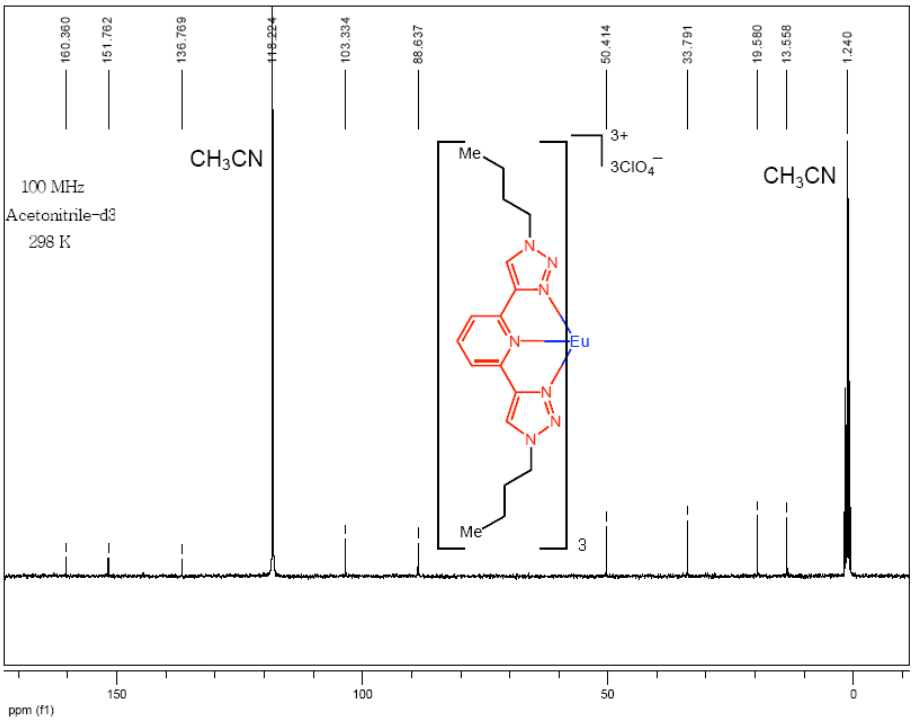

Figure S34. Full ^{13}C NMR spectrum (100 MHz, CD_3CN) of $[Eu(\mathbf{2})_3]^{3+}$.

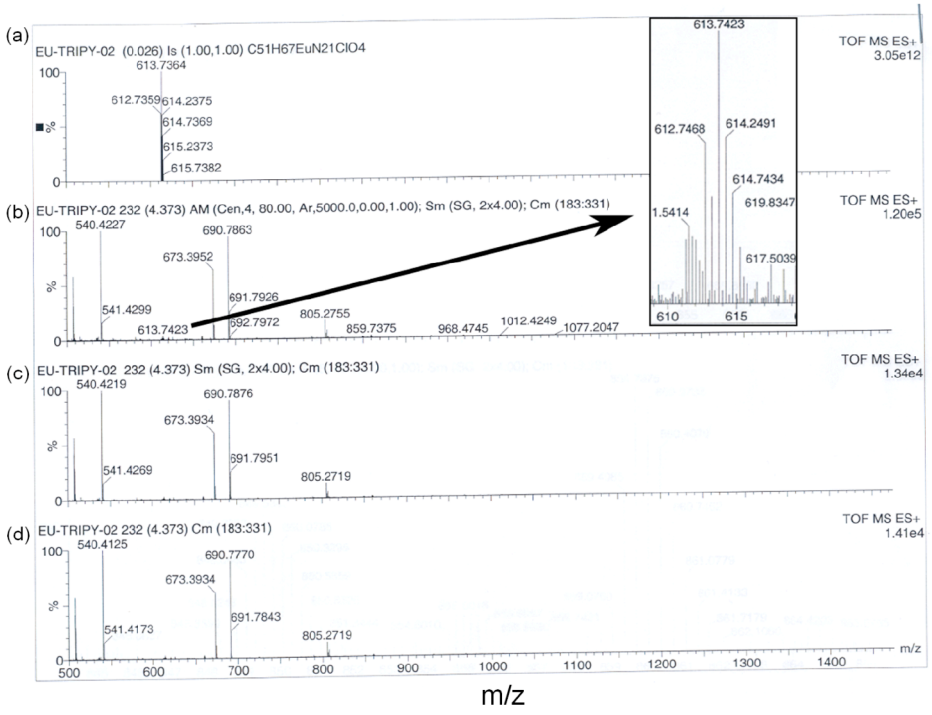

Figure S35. Theoretical HiRes ESI spectra of (a) the $(M–2ClO_4)^{+2}$ ion is observed in (b,c,d) the actual sample data of $[Eu(\mathbf{2})_3]•3ClO_4$.

S.9. REFERENCES

1 B. A. Dana, B. H. Robinson, and J. Simpson, *J. Organomet. Chem.*, 2002, **648**, 251.

2 V. Aucagne, K. D. Hänni, D. A. Leigh, P. J. Lusby and D. B. Walker, *J. Am. Chem. Soc.*, 2006, **128**, 2186.

3 J. H. Boyer and J. Hamer, *J. Am. Chem. Soc.*, 1955, **77**, 951.

4 I. P. Evans, A. Spencer and G. Wilkinson, *J. Chem. Soc., Dalton Trans.*, 1973, 204.

5 An empirical correction for absorption anisotropy, see: R. Blessing, *Acta Cryst. A*, **1995**, *51*, 33.

6 SAINT 6.1, Bruker Analytical X-Ray Systems, Madison, WI.

7 SHELXTL-Plus V5.10, Bruker Analytical X-Ray Systems, Madison, WI.

8 E. C. Constable, *Adv. Inorg. Chem.*, 1986, **30**, 69.

9 G. A. Jeffrey, *An Introduction to Hydrogen Bonding*, Oxford University Press, New York, 1997.

10 T. Steiner and W. Saenger, *Acta Cryst. B*, 1992, **48**, 819.

11 R. D. Chapman, R. T. Loda, J. P. Riehl and R. W. Schwartz, *Inorg. Chem.*, 1984, **23**, 1652.

12 (*a*) S. Petoud, J. C. G. Bünzli, T. Glanzman, C. Piguet, Q. Xiang and R. P. Thummel, *J. Luminesc.*, 1999, **82**, 69; (*b*) H. R. Mürner, E. Chassat, R. P. Thummel and J. C. G. Bünzli, *J. Chem. Soc., Dalton Tans.*, 2000, 2809.

13 (*a*) M. D. Lind, J. L. Hoard, M. J. Hamor, T. A. Hamor and J. L. Hoard, *Inorg. Chem.*, 1964, **3**, 34; (*b*) G. H. Cohen and J. L. Hoard, *J. Am. Chem. Soc.*, 1966, **88**, 3228; (*c*) E. Fleisceh and S. Hawkinson, *J. Am. Chem. Soc.*, 1967, **89**, 720; (*d*) X. Solnas and M. F. Altaba, *Acta Cryst. C*, 1984, **40**, 635; (*e*) J. M. Lopex-Alcala, M. C. Puerta-Vizcaino, G. Gonzalez-Vilchez, E. Duesler and R. E. Tapscott, *Acta Cryst. C*, 1984, **40**, 939; (*f*) X. Solnas, M. Font-Altaba and J. Garcia-Oricain, *Acta Cryst. C*, 1985, **41**, 525; (*g*) M. Mizuno, S. Funahashi, N. Nakasuka and M. Tanaka, *Inorg. Chem.*, 1991, **30**, 1550; (h) T. Mizuta, J. Wang and K. Miyoshi, *Bull. Chem. Soc. Jpn.*, 1993, **66**, 2547; (*i*) T. Mizuta, J. Wang and K. Miyoshi, *Inorg. Chim. Acta*, 1995, **230**, 119; (*j*) S. Seibig and R. van Eldik,

Inorg. Chim. Acta, 1998, **279**, 37; (*k*) R. Meier, S. A. Bedell and G. Henkel, *Inorg. Chim. Acta*, 2002, **337**, 337; (*l*) I. Ivanovic-Burmazovic, M. S. A. Hamza and R. van Eldik, *Inorg. Chem.*, 2002, **41**, 5150.

14 (*a*) For a 7-coordinate Ru(II) crystal structure, see: D. C. Liles and P. F. M. Verhoeven, *J. Organomet. Chem.*, 1996, **522**, 33. For 7-coordinate ruthenium centers that are inferred from experimental data, see: (*b*) S. M. Maddock, C. E. F. Rickard, W. Roper, and L. J. Wright, *J. Organomet. Chem.*, 1996, **510**, 267; (*c*) D. G. Gusev, R. Hubener, P. Burger, O. Orama and H. Berke, *J. Am. Chem. Soc.*, 1997, **119**, 3716; (*d*) S. M. Ng, W. H. Lam, C. C. Mak, C. W. Tsang, G. Jia, Z. Lin and C. P. Lau, *Organomet.*, 2003, **22**, 641; (*e*) M. Murali and M. Palaniandavar, *Dalton Trans.*, 2006, 730.

15 (*a*) B. A. Moyer and T. J. Meyer, *Inorg. Chem.*, 1981, **20**, 436; (*b*) K.-I. Okamoto, J. Hidaka, I. Iida, K. Higashino and K. Kanamori, *Acta Cryst. C*, 1990, **46**, 2327; (*c*) A. Dovletoglou, S. A. Adeyemi and T. J. Meyer, *Inorg. Chem.*, 1996, **35**, 4120.

16 C. Creutz, M. Chou, T. L. Netzel, M. Okumura and N. Sutin, *J. Am. Chem. Soc.*, 1980, **102**, 1309.

17 E. Tfouni, K. Q. Ferreira, F. G. Doro, R. S. da Silva and Z. N. da Rocha, *Coord. Chem. Rev.*, 2005, **249**, 405.